

Cosmological Insights into the Early Accretion of *r*-process-enhanced Stars. I. A Comprehensive Chemodynamical Analysis of LAMOST J1109+0754

Mohammad K. Mardini^{1,2}, Vinicius M. Placco³, Yohai Meiron⁴, Marina Ishchenko⁵, Branislav Avramov⁶ Matteo Mazzarini⁶, Peter Berczik^{5,6,7}, Manuel Arca Sedda⁶, Timothy C. Beers^{8,9}, Anna Frebel^{9,10}, Ali Taani¹¹, Martina Donnari ¹², Mashhoor A. Al-Wardat ^{13,14}, and Gang Zhao ^{1,2} ¹ Key Lab of Optical Astronomy, National Astronomical Observatories, Chinese Academy of Sciences, Beijing 100101, People's Republic of China gzhao@nao.cas.cn ² Institute of Space Sciences, Shandong University, Weihai 264209, People's Republic of China NSF's Optical-Infrared Astronomy Research Laboratory, Tucson, AZ 85719, USA ⁴ Department of Astronomy and Astrophysics, University of Toronto, 50 St. George Street, Toronto, ON M5S 3H4, Canada ⁵ Main Astronomical Observatory, National Academy of Sciences of Ukraine, 27 Akademika Zabolotnoho St., 03143 Kyiv, Ukraine ⁶ Astronomisches Rechen Institut—Zentrum für Astronomie der Universität Heidelberg, Mönchhofstrasse 12-14, D-69120 Heidelberg, Germany ⁷ National Astronomical Observatories and Key Laboratory of Computational Astrophysics, Chinese Academy of Sciences, 20A Datun Road, Chaoyang District, Beijing 100101, People's Republic of China ⁸ Department of Physics, University of Notre Dame, Notre Dame, IN 46556, USA JINA Center for the Evolution of the Elements (JINA-CEE), USA ¹⁰ Department of Physics and Kavli Institute for Astrophysics and Space Research, Massachusetts Institute of Technology, Cambridge, MA 02139, USA Physics Department, Faculty of Science, Al-Balqa Applied University, Jordan ¹² Max-Planck-Institut für Astronomie, Königstuhl 17, 69117 Heidelberg, Germany

¹³ Department of Applied Physics and Astronomy, University of Sharjah, Sharjah, United Arab Emirates ¹⁴ Sharjah Academy for Astronomy, Space Sciences and Technology, University of Sharjah, Sharjah, United Arab Emirates Received 2020 August 3; revised 2020 September 20; accepted 2020 September 24; published 2020 November 6

Abstract

This study presents a comprehensive chemodynamical analysis of LAMOST J1109+0754, a bright (V=12.8), extremely metal-poor ([Fe/H] = -3.17) star, with a strong r-process enhancement ([Eu/Fe] = $+0.94\pm0.12$). Our results are based on the 7D measurements supplied by Gaia and the chemical composition derived from a high-resolution ($R\sim110,000$), high signal-to-noise ratio (S/N ~60) optical spectrum obtained by the 2.4 m Automated Planet Finder Telescope at Lick Observatory. We obtain chemical abundances of 31 elements (from lithium to thorium). The abundance ratios ([X/Fe]) of the light elements ($Z\leqslant30$) suggest a massive Population III progenitor in the 13.4– $29.5\,M_\odot$ mass range. The heavy-element ($30 < Z \leqslant 90$) abundance pattern of J1109+075 agrees extremely well with the scaled-solar r-process signature. We have developed a novel approach to trace the kinematic history and orbital evolution of J1109+0754 with a cOsmologically deRIved timE-varyiNg Galactic poTential (the ORIENT) constructed from snapshots of a simulated Milky Way analog taken from the Illustris-TNG simulation. The orbital evolution within this Milky Way-like galaxy, along with the chemical abundance pattern, implies that J1109+0754 likely originated in a low-mass dwarf galaxy located $\sim60\,\mathrm{kpc}$ from the center of the Galaxy, which was accreted $\sim6-7\,\mathrm{Gyr}$ ago, and that the star now belongs to the outer-halo population.

Unified Astronomy Thesaurus concepts: Chemically peculiar stars (226); Population III stars (1285); R-process (1324); Stellar kinematics (1608); Chemical abundances (224); Stellar dynamics (1596); Orbits (1184); Galaxy dynamics (591)

Supporting material: machine-readable table

1. Introduction

Since the pioneering work of Burbidge et al. (1957) and Cameron (1957), numerous studies have focused attention on the astrophysical site(s) of the rapid neutron-capture process (*r*-process). Although full understanding has not yet been achieved, several promising mechanisms have been proposed, including (i) the innermost ejecta of regular core-collapse supernovae (e.g., Sato 1974; Witti et al. 1994; Farouqi et al. 2010; Mirizzi 2015), (ii) the outer layers of supernova explosions (e.g., Thielemann et al. 1979; Cowan et al. 1983; Nadyozhin & Panov 2007; Qian 2014), (iii) magnetorotational jet-driven supernovae (e.g., Symbalisty et al. 1985; Fujimoto et al. 2008; Nishimura et al. 2015; Obergaulinger et al. 2018), (iv) neutron star mergers (NSMs; e.g., Symbalisty & Schramm 1982; Rosswog et al. 2000; Eichler et al. 2015; Thielemann et al. 2017), and (v) collapsars (Siegel et al. 2019).

Observationally, the advanced LIGO-Virgo detectors collected the first gravitational wave signature from the merger of a binary neutron star system (GW170817; Abbott et al. 2017b), with subsequent electromagnetic follow-up (photometric and spectroscopic) observations of its associated kilonova (SSS17a; e.g., Drout et al. 2017; Kilpatrick et al. 2017; Shappee et al. 2017), providing a prime example of multimessenger astronomy (e.g., Abbott et al. 2017a; Goldstein et al. 2017; Savchenko et al. 2017; Soares-Santos et al. 2017). These kilonova observations provided strong evidence for the existence of at least one site for the astrophysical operation of the r-process, namely, NSMs (e.g., Côté et al. 2017; Cowperthwaite et al. 2017). Even before this detection, support for NSMs as a potential major source of r-process elements was found with the discovery of the ultrafaint dwarf galaxy Reticulum II (Ji et al. 2016), which contains almost exclusively r-process-enhanced (RPE) metal-poor stars (see more details below) that appear to have originated in this system from

gas that had been enriched by a prior, prolific *r*-process event that polluted this galaxy. Models of the yields suggested this event to have been an NSM, but other sources might also have contributed.

Interestingly, Placco et al. (2020) recently analyzed the moderately *r*-process- and CNO-enhanced star RAVE J1830 –4555, whose neutron-capture abundance pattern matches both the fast ejecta yields of an NSM and the yields of a rotating massive star experiencing an *r*-process event during its explosion. Magnetorotational supernovae have been suggested as viable astrophysical environments for the main *r*-process to operate (e.g., Nishimura et al. 2017; Halevi & Mösta 2018; Obergaulinger et al. 2018; Côté et al. 2019), but more discriminating model predictions are needed to make progress, in addition to more observations, to fully investigate these (multiple) progenitor sources. This is supported by the overall observed levels of [Eu/Fe]¹⁵ in the body of data of, e.g., metal-poor stars, which suggests that more than just one source is responsible for the *r*-process inventory of the universe.

In particular, constraints can be uniquely obtained from individual Galactic halo stars with enhancements in *r*-process elements—the so-called RPE stars—to provide novel insights into this long-standing issue (for a selected list see, e.g., Sneden et al. 1996; Hill et al. 2002; Hansen et al. 2012; Placco et al. 2017; Hawkins & Wyse 2018; Roederer et al. 2018; Sakari et al. 2018a, 2018b, 2019; Placco et al. 2020, and references therein).

Substantial recent efforts have been underway to increase the numbers of the known RPE metal-poor stars (Christlieb et al. 2004; Barklem et al. 2005; Mardini et al. 2019a), including that of the *R*-Process Alliance (RPA; Hansen et al. 2018; Sakari et al. 2018a; Ezzeddine et al. 2020; Holmbeck et al. 2020), which has recently identified a total of 72 new *r*-II and 232 new *r*-I stars. ¹⁶ This has increased the number of RPE stars known to 141 *r*-II and 345 *r*-I stars. Here we report on a detailed analysis of LAMOST J110901.22+075441.8 (hereafter J1109+0754), an *r*-II star with strong carbon enhancement, originally identified by Li et al. (2015). J1109+0754 thus adds to the sample of well-studied RPE stars.

It is now widely recognized that the halo of the Milky Way experienced mergers with small dwarf galaxies and grew hierarchically as a function of time (e.g., Searle & Zinn 1978; White & Rees 1978; Davis et al. 1985). Some of these galaxies have survived, some experienced strong structural distortions, and some have been fully disrupted. Since the discovery of Reticulum II (Ji et al. 2016), it has become clear that at least some of the halo RPE stars must have originated in small satellite dwarf galaxies (Brauer et al. 2019) before their eventual accretion into the Galactic halo. Therefore, combining chemical compositions of RPE stars with the results from kinematic analyses and/or results from cosmological simulations can help to assess the cosmic origin of these stars, in addition to learning about the formation and evolution of the Milky Way (e.g., Roederer et al. 2018; Mardini et al. 2019a; D. Gudin et al. 2020, in preparation). The orbital integrations of halo stars reported in the literature, including those of RPE stars (e.g., Roederer et al. 2018; Mardini et al. 2019a), are usually determined with a fixed Galactic potential (e.g., MWPotential2014; Bovy 2015). This fixed Galactic potential

provides a snapshot view of the present-day dynamical parameters of, e.g., RPE stars, but in order to gain detailed insights into the stars' orbital histories in a more realistic way, a *time-varying* Galactic potential should be considered. In this study, we explore a time-varying Galactic potential, based on a simulated Milky Way analog extracted from the Illustristing simulation (Rodriguez-Gomez et al. 2015; Marinacci et al. 2018; Naiman et al. 2018; Nelson et al. 2018, 2019a, 2019b; Pillepich et al. 2018, 2019; Springel et al. 2018). This allows us to gain a more complete picture of the orbital evolution of J1109+0754.

Cosmological simulations can nowadays be carried out with a sufficiently large number of tracer particles such that Milky Way–sized halos can be well resolved, including both their baryonic components (gas and stars). By identifying halos in the simulation box that are representative of the Milky Way, we aim at mapping the evolution of the orbit of J1109+0754 to learn about its possible origin scenario.

This paper is organized as follows. We describe the observational data in Section 2. Section 3 presents the determinations of stellar parameters. The chemical abundances are addressed in Section 4. The possible pathways that may have led to the formation of J1109+0754 are described in Section 5. The kinematic signature and orbital properties of J1109+0754 are discussed in Section 6. Our conclusions are presented in Section 7.

2. Observations

The metal deficiency of J1109+0754 was first reported in the third data release (DR3¹⁷) of the Large Sky Area Multi-Object Fiber Spectroscopic Telescope (LAMOST) survey (Zhao et al. 2006, 2012; Cui et al. 2012). This relatively bright (V=12.8) K-giant star was originally followed up with high-resolution spectroscopy on 2014 May 9, using the SUBARU telescope and the echelle High Dispersion Spectrograph (HDS; Noguchi et al. 2002). The analysis of this high-resolution spectrum confirms the star's extremely low metallicity and strong enhancement in r-process elements (Li et al. 2015).

On 2015 May 14, J1109+0754 was also observed with the Automated Planet Finder Telescope (APF; we refer the reader to more details about the target selection and the overall scientific goals in Mardini et al. 2019a). The observing setup yielded a spectral resolving power of $R \sim 110,000$. Note that our initial sample was selected according to the stars' corresponding Lick indices, as part of a sample of 20 stars observed with APF. Data for 13 of those stars had sufficient S/N to allow for a reliable analysis, including J1109+0754. The results of the remaining 12 newly discovered stars were reported in Mardini et al. (2019a, 2019b). Due to the reduced wavelength coverage of the SUBARU spectrum, relatively few neutron-capture elements could be detected. Therefore, we decided to carry out a detailed analysis of the APF spectrum of J1109+0754 to complete its abundance assay and link it to the star's kinematics. Table 1 lists the basic data for J1109+0754.

We used IRAF (Tody 1986, 1993) to carry out a standard echelle data reduction (including bias subtraction, cosmic-ray removal, wavelength calibration, etc.). Our final APF spectrum covers a wide wavelength range (\sim 3730–9989 Å) and has a fairly good signal-to-noise ratio (S/N per pixel \sim 60 at 4500 Å). We measured the radial velocity (RV) of J1109+0754 in the same

 $[\]overline{^{15}}$ [X/Y] = log(N_X/N_Y)_{*} - log(N_X/N_Y)_©, where N is the number density of atoms of elements X and Y in the star (*) and the Sun (⊙), respectively.

 $^{^{16}}$ r-II stars are defined as [Eu/Fe] > +1.0 and [Ba/Eu] < 0, while r-I stars are defined as $+0.3 < [Eu/Fe] \le +1.0$ and [Ba/Eu] < 0.

¹⁷ http://dr3.lamost.org

Table 1Basic Data for LAMOST J1109+0754

Quantity	Symbol	Value	Units	Reference
R.A.	α (J2000)	11:09:01.22	hh:mm:ss.ss	SIMBAD
Decl.	δ (J2000)	+07:54:41.8	dd:mm:ss.s	SIMBAD
Galactic longitude	ℓ	246.5691	degrees	This study
Galactic latitude	b	59.0610	degrees	This study
Parallax	$\overline{\omega}$	0.0717 ± 0.0442	mas	Lindegren et al. (2018)
Distance	D	$4.91^{+0.85}_{-0.69}$	kpc	Bailer-Jones et al. (2018)
Proper motion (α)	PMRA	2.009 ± 0.0748	$\mathrm{mas}\ \mathrm{yr}^{-1}$	Lindegren et al. (2018)
Proper motion (δ)	PMDec	-9.155 ± 0.0652	mas yr ⁻¹	Lindegren et al. (2018)
Mass	M	0.75 ± 0.20	M_{\odot}	Assumed
B magnitude	B	13.361 ± 0.009	mag	Henden et al. (2016)
V magnitude	V	12.403 ± 0.016	mag	Henden et al. (2016)
J magnitude	J	10.443 ± 0.024	mag	Skrutskie et al. (2006)
K magnitude	K	9.783 ± 0.027	mag	Skrutskie et al. (2006)
Color excess	E(B-V)	0.0251 ± 0.0005	mag	Neugebauer et al. (1984) ^a
Bolometric correction	BC_V	-0.45 ± 0.07	mag	This study, based on Alonso et al. (1999)
Effective temperature	$T_{ m eff}$	4633 ± 150	K	This study, based on Frebel et al. (2013)
Log of surface gravity	$\log g$	0.96 ± 0.30	dex	This study, based on Frebel et al. (2013)
Microturbulent velocity	$v_{\rm t}$	2.20 ± 0.30	${\rm km}~{\rm s}^{-1}$	This study, based on Frebel et al. (2013)
Metallicity	[Fe/H]	-3.17 ± 0.09		This study, based on Frebel et al. (2013)
Radial velocity	RV	-100.2 ± 1.02	${\rm km}~{\rm s}^{-1}$	APF (MJD: 57132.229)
•	RV	-98.64 ± 0.52	${\rm km}~{\rm s}^{-1}$	Lindegren et al. (2018)
	RV	-99.05 ± 0.40	${\rm km}~{\rm s}^{-1}$	SUBARU (MJD: 56786.294, Li et al. 2015)
	RV	-102.9 ± 1.41	${\rm km~s}^{-1}$	LAMOST (MJD: 581449.000, private communication)
Natal carbon abundance	[C/Fe]	$+0.66 \pm 0.27$		This study, based on Placco et al. (2014)

Notes.

way described in Mardini et al. (2019b). We employed a synthesized template for the cross-correlation against the final reduced spectrum of J1109+0754; using the Mg I line triplet (at $\sim\!5160\text{--}5190\,\text{ Å}$). This yielded RV = $82.39\pm0.8\,\mathrm{km\,s^{-1}}$. In addition, J1109+0745 has some other RV measurements in the literature (see Table 1). These measurements do not suggest the presence of an unseen binary companion; however, they do not exclude the possibility of a long-period binary.

3. Determinations of Stellar Parameters

We employed the TAME code (for more details, see Kang & Lee 2015) to measure the equivalent widths (hereafter EWs) for 209 unblended lines of light elements ($Z \leq 30$), with the exception of Li, C, O, Na, and the two strong Mg lines at 5172 and 5183 Å whose abundances we obtained from spectrum synthesis. We then applied the most recent version of the LTE stellar analysis code MOOG (Sneden 1973; Sobeck et al. 2011) and one-dimensional α -enhanced ([α /Fe] = +0.4) atmospheric models (Castelli & Kurucz 2003) to derive individual abundances from these lines. Table 2 lists the atomic data used in this work, the measured EWs, and the derived individual abundances, including those from spectrum synthesis.

We employed 99 Fe I and 12 Fe II lines, which were used to spectroscopically determine the stellar parameters of J1109 \pm 0754. We reduced the slope of the derived individual line abundances of the Fe I lines as a function of their excitation potentials (see Table 2) to its minimum value in order to determine the effective temperature ($T_{\rm eff}$). By fixing the value of $T_{\rm eff}$ and also removing the trend between the individual abundances of Fe I lines and reduced EW, we determine the

microturbulent velocity (v_t). The surface gravity ($\log g$) was obtained by matching the average abundance of the Fe I and Fe II lines. This procedure yielded $T_{\rm eff}=4403$ K, $\log g=0.11$, and $v_t=2.87$ km s⁻¹. These stellar parameters were used as inputs for the empirical calibration described in Frebel et al. (2013) to adjust $T_{\rm eff}$ to the photometric scale. This yielded final stellar parameters of $T_{\rm eff}=4633$ K, $\log g=0.96$, [Fe/H] = -3.17, and $v_t=2.20$ km s⁻¹, listed in Table 1. We adopt these parameters in our remaining analysis.

We also employed the empirical metallicity-dependent color $-T_{\rm eff}$ relation presented by Alonso et al. (1999) to calculate the photometric $T_{\rm eff}$ of J1109+0754. We adopted total Galactic reddening along the line of sight to J1109+0754 of $E(B-V)=0.025\pm0.001$ (Neugebauer et al. 1984). We generated 10,000 sets of parameter estimates, by resampling each input photometric information (the B, V, J, K magnitudes, E(B-V)), along with [Fe/H]. We adopted the median of each calculation as the final results, and the 16th and 84th percentiles (the subscript and superscript, respectively) as the uncertainties. These calculations yielded $T_{\rm eff}(V-J)=4575^{33}_{31}$ K and $T_{\rm eff}(V-K)=4521^{26}_{26}$ K. These results are consistent, within 1σ , with the final $T_{\rm eff}$ of 4633 K derived from the spectroscopic method.

4. Chemical Abundances

We employed both EW analysis ¹⁸ and spectral synthesis applied to the APF spectrum to derive the chemical abundances (and upper limits) for a total of 31 elements, including 16

^a https://irsa.ipac.caltech.edu/applications/DUST/

^b Determined in the same manner presented in Mardini et al. (2019a).

 $[\]overline{\ }^{18}$ Abundances were derived using MOOG's abfind driver.

Table 2
Lines, Atomic Data, EWs, and Individual Abundances

Li I	6707.749	0.000			
LII		0.000	-0.804	Syn	<-0.02
C(CH)	4214.000	•••		Syn	5.16
O I	6300.300	0.000	-9.820	Syn	6.57
Na I	5889.951	0.000	0.120	Syn	3.37
Na I	5895.924	0.000	-0.180	Syn	3.26
Mg I	4167.270	4.350	-0.710	26.73	4.89
Mg I	4571.100	0.000	-5.690	55.76	5.06
Mg I	4702.990	4.330	-0.380	40.76	4.72
Mg I	5172.684	2.710	-0.400	Syn	5.13
Mg I	5183.604	2.715	-0.180	Syn	5.13
Mg I	5528.400	4.340	-0.500	47.11	4.86
Ca I	4283.010	1.890	-0.220	36.58	3.55
Ca I	4318.650	1.890	-0.210	34.42	3.49
Ca I	4425.440	1.880	-0.360	23.97	3.38
Ca I	4435.690	1.890	-0.520	49.12	4.04
Ca I	4454.780	1.900	0.260	55.33	3.38
Ca I	4455.890	1.900	-0.530	25.32	3.60
Ca I	5265.560	2.520	-0.260	16.32	3.72
Ca I	5588.760	2.520	0.210	27.50	3.51
Ca I	5594.470	2.520	0.100	17.49	3.37
Ca I	5598.490	2.520	-0.090	14.67	3.47
Ca I	5857.450	2.930	0.230	11.27	3.49
Ca I	6102.720	1.880	-0.790	22.20	3.59
Ca I	6122.220	1.890	-0.310	38.10	3.44
Ca I	6162.170	1.900	-0.090	52.97	3.47
Ca I	6439.070	2.520	0.470	36.24	3.36
Sc II	4314.080	0.620	-0.100	81.98	0.07
Sc II	4325.000	0.600	-0.440	64.78	0.05
Sc II	4400.390	0.610	-0.540	49.85	-0.12

(This table is available in its entirety in machine-readable form.)

neutron-capture elements. The line lists for spectrum synthesis were generated with the linemake code. ¹⁹ The final adopted abundances are listed in Table 3. We use the solar abundances from Asplund et al. (2009) to calculate [X/H] and [X/Fe] ratios (where X denotes different elements). The standard deviation of the mean (σ), number of the lines used ($N_{\rm lines}$), and solar abundances ($\log \varepsilon_{\odot}$) are also listed in Table 3. In the following, we comment on measurement details of individual elements and groups of elements. In Section 5, we further discuss the results and the abundance trends.

4.1. Lithium

J1109+0754 is on the upper red giant branch, suggesting that some elements present in the stellar atmosphere have been altered owing to the first dredge-up and other mixing processes. Lithium is affected by these processes, and its abundance is expected to be depleted compared to the Spite plateau value (e.g., Kirby et al. 2016). This results in a weakened lithium doublet line at 6707 Å, making the derivation of an accurate abundance a challenge. Hence, we were only able to derive an upper limit using spectral synthesis. Our low upper limit of A(Li) < -0.02 agrees well with lithium values of other cool giants with similar temperatures (Roederer et al. 2014).

Table 3
Abundances of J1109+0754

Species	$\log \varepsilon (X)$	[X/H]	[<i>X</i> /Fe]	σ (dex)	$N_{\rm lines}$	$\log arepsilon_{\odot}^{\mathbf{a}}$
Li I	<-0.02	<-1.07	<2.10		1	1.05
C (CH)	+5.16	-3.27	-0.10	0.10		8.43
O I	+6.57	-2.12	+1.05	0.10	1	8.69
Na I	+3.32	-2.92	+0.24	0.08	2	6.24
Mg I	+4.96	-2.64	+0.53	0.17	6	7.60
Ca I	+3.52	-2.82	+0.35	0.17	15	6.34
Sc II	+0.01	-3.14	+0.03	0.08	6	3.15
Ti I	+2.08	-2.87	+0.30	0.17	18	4.95
Ti II	+2.08	-2.87	+0.30	0.17	35	4.95
VI	+0.69	-3.24	-0.07	0.12	2	3.93
Cr I	+2.04	-3.60	-0.43	0.17	6	5.64
Mn I	+1.68	-3.75	-0.58	0.18	4	5.43
Fe I	+4.33	-3.17	0.00	0.09	99	7.50
Fe II	+4.33	-3.17	0.00	0.07	12	7.50
Co I	+2.03	-2.96	+0.21	0.20	3	4.99
Ni I	+3.01	-3.21	-0.04	0.03	3	6.22
Zn I	+1.76	-2.80	+0.37	0.11	2	4.56
Sr I	+0.05	-2.82	+0.35	0.10	1	2.87
Sr II	-0.05	-2.92	+0.25	0.07	2	2.87
Y II	-0.91	-3.12	+0.05	0.07	6	2.21
Zr II	-0.21	-2.79	+0.38	0.06	2	2.58
Ba II	-0.74	-2.92	+0.25	0.21	4	2.18
La II	-1.52	-2.62	+0.55	0.13	6	1.10
Ce II	-1.24	-2.82	+0.35	0.10	1	1.58
Pr II	-1.67	-2.39	+0.78	0.10	1	0.72
Nd II	-1.11	-2.53	+0.64	0.11	8	1.42
Sm II	-1.30	-1.99	+1.18	0.06	7	0.69
Eu II	-1.71	-2.23	+0.94	0.12	4	0.52
Gd II	< -1.00	< -2.07	<+1.10	•••	1	1.07
Tb II	-1.74	-2.04	+1.13	0.11	2	0.30
Dy II	-1.00	-2.10	+1.07	0.09	2	1.10
Er II	-1.50	-2.42	+0.75	0.10	1	0.92
Hf II	< -1.22	< -2.07	<+1.10	•••	1	0.85
Th II	< -2.05	< -2.07	<+1.10	•••	1	0.02

Note.

4.2. Carbon and Nitrogen

Shortly after stars leave the main sequence and begin to ascend the giant branch, nucleosynthesis reactions in the core (e.g., the CN cycle) are expected to modify a number of the surface-element abundances (e.g., carbon, nitrogen, and oxygen). The most basic interpretation of the observed carbon and nitrogen, in evolved stars, is that their outer convective envelope expands and penetrates the CN-cycled interior through convective flows, which leads to an increase in the observed surface nitrogen and depletion in the surface carbon abundances (e.g., Hesser 1978; Genova & Schatzman 1979; Charbonnel 1995; Gratton et al. 2000; Spite et al. 2006; Placco et al. 2014). However, when stars evolve past the luminosity bump, nonconvective mixing can still be considered a viable source for dilution (Thomas 1967; Iben 1968).

We determined carbon abundances and isotope ratios ($^{12}\text{C}/^{13}\text{C}$) from spectrum synthesis by matching two portions of the CH G band at 4280 and 4217 Å with synthetic spectra of varying abundances and isotope ratios. This yielded a best-fit carbon abundance $\log \epsilon(\text{C}) = 5.16 \pm 0.10$ ([C/Fe] = -0.10) and an isotopic ratio $^{12}\text{C}/^{13}\text{C} = 2.0 \pm 2.0$. This low $^{12}\text{C}/^{13}\text{C}$ ratio suggests that a significant amount of ^{12}C has been converted into ^{13}C . Figure 1 shows the line fits used to obtain the carbon abundance and the $^{12}\text{C}/^{13}\text{C}$ isotopic ratios (top

¹⁹ https://github.com/vmplacco/linemake

^a Solar photospheric abundances from Asplund et al. (2009).

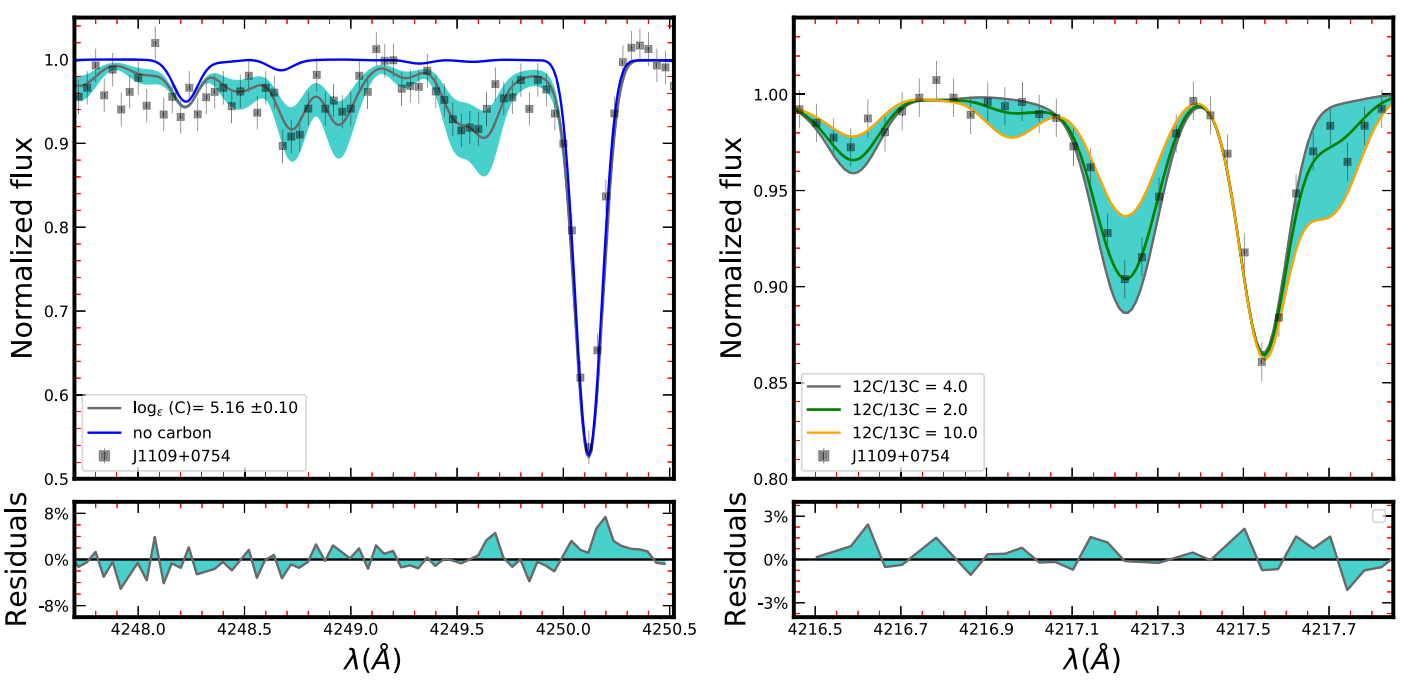


Figure 1. Left panel: portion of the J1109+0754 spectrum near the CH G band. The filled squares indicate the observed data, and the solid red line denotes the best-fit carbon abundance. The turquoise shaded region encloses a ± 0.10 dex difference in $\log \epsilon$ (C). Right panel: determination of the carbon isotopic ratio 12 C/ 13 C. The filled squares indicate the observed data, and the solid red line is the best-fit isotopic ratio. The bottom panels represent the residuals between the best fits and the observed data.

panels) and the residuals between the observed spectrum and the adopted best fits (bottom panels). We use upper and lower carbon abundance fits $(\pm 0.10 \, \text{dex})$ to assess the abundance uncertainty on the isotope ratio.

Although we expected that J1109+0754 would exhibit an enhancement in its nitrogen abundance, we could not reliably detect any CN features in the APF spectrum and thus determine a meaningful upper limit.

4.3. Elements from Oxygen to Zinc

We determined the atmospheric abundance of the light elements with different methods based on the availability of nonblended features with reliable continuum estimates. We only used EW analysis to derive the abundances of Ca, Sc, Ti, V, Cr, Mn, Co, Ni, and Zn. We used a combination of EW and spectrum synthesis matching to measure the magnesium abundance. The O (at $6300\,\text{Å}$) and Na (at 5889 and $5895\,\text{Å}$) were determined just from spectrum synthesis. Table 2 lists the atomic data, the measured EWs, and the atmospheric abundances for each individual line. Table 3 lists the adopted average abundances.

4.4. Neutron-capture Elements

We used spectrum synthesis to measure the abundances and upper limits for 16 neutron-capture elements (from Sr to Th). Where applicable, we took into account line broadening due to isotope shifts and hyperfine splitting structure.²⁰

Figure 2 shows portions of the spectrum of J1109+0754 around the Ba II line at 4554 Å and the Eu II line at 4129 Å and illustrates our technique of finding a best fit to the line. Spectra matching the noise level of the line and continuum are used to determine the uncertainties.

We were able to measure the abundances for three elements that belong to the first r-process peak, Sr, Y, and Zr. The abundances of strontium were measured using transitions from two different ionization stages (Sr I at 4607.331 Å and Sr II at 4077.714 and 4215.524 Å); the results agree within 0.10 dex. The abundances determined for yttrium, using six lines (4235.731, 4358.727, 4883.684, 4900.110, 5087.420, and 5205.731 Å), agree within 1σ . For zirconium, we measured $\log \epsilon$ (Zr) = -0.17 and -0.25, using the two lines at 4149.198 and 4161.200 Å, respectively.

There are many absorption lines for neutron-capture elements within the spectral range of our data. However, many lines are located in blue regions with poor S/N, and some are heavily blended. Therefore, we used eight lines to measure $\log \epsilon$ (Nd) = -1.11, seven lines for $\log \epsilon$ (Sm) = -1.30, six lines for $\log \epsilon$ (La) = -1.52, four lines for $\log \epsilon$ (Ba) = -0.74 and $\log \epsilon$ (Eu) = -1.71, two lines for $\log \epsilon$ (Tb) = -1.74 and $\log \epsilon$ (Dy) = -1.00, and one line for $\log \epsilon$ (Ce) = -1.24, $\log \epsilon$ (Pr) = -1.67, and $\log \epsilon$ (Er) = -1.50, and we obtained upper limits for $\log \epsilon$ (Gd) = <-1.0, $\log \epsilon$ (Hf) = <-1.2, and $\log \epsilon$ (Th) = <-2.4. Generally, line abundances for each element agree well with each other, which is reflected in the small reported standard deviations. Table 3 lists our final abundances for all elements.

4.5. Systematic Uncertainties

Table 4 lists the systematic uncertainties, as derived from varying the uncertainties of the adopted atmospheric models (Δ $T_{\rm eff}=\pm150~{\rm K}, \Delta\log g=\pm0.30~{\rm dex},$ and $\Delta \nu_{\rm t}=\pm0.30~{\rm km~s}^{-1})$ one at the time. We then recalculated our abundances. We take the differences as our final systematic uncertainties.

We also attempted to quantify systematic uncertainties associated with our measurement technique by comparing our results to those of Li et al. (2015). However, only a comparison of

²⁰ Hyperfine structure information can be found in https://github.com/vmplacco/linemake/blob/master/README.md.

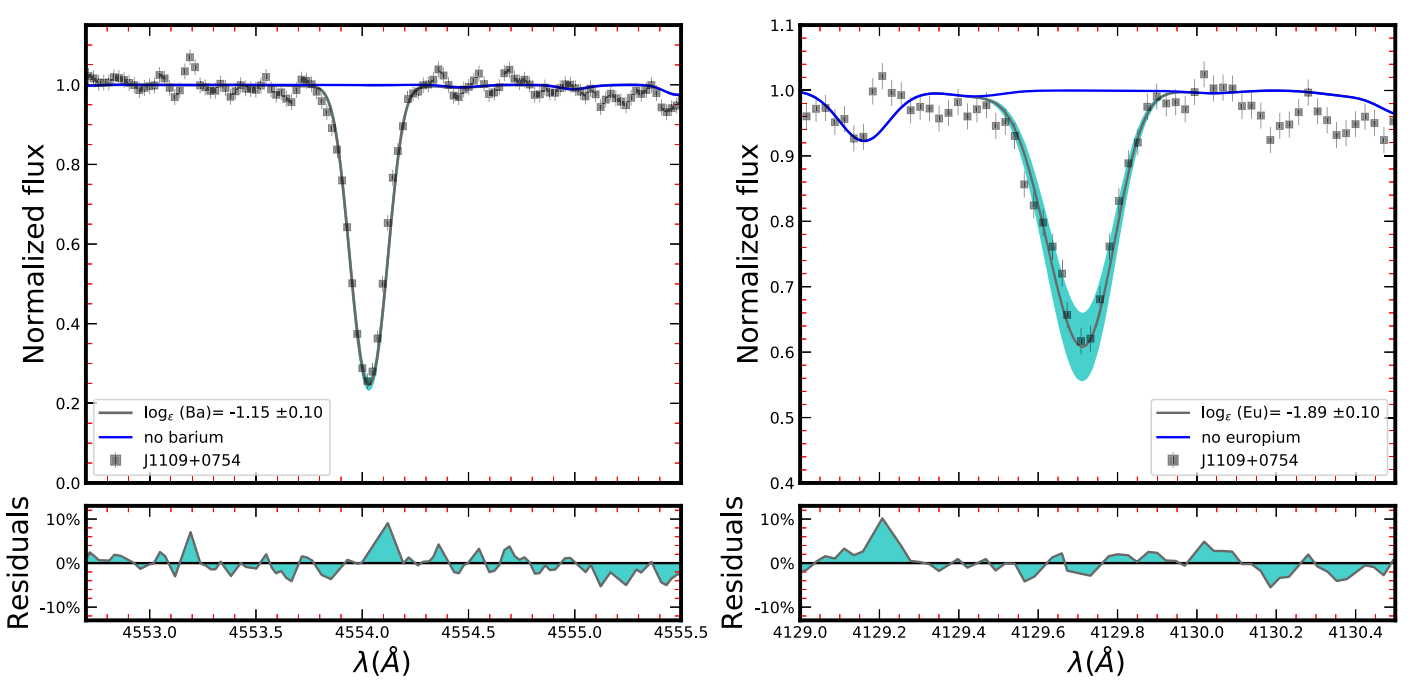


Figure 2. Portions of the J1109+0754 spectrum near the Ba II line at 4554 Å (left panel) and the Eu II line at 4129 Å. Best-fit abundances obtained with spectrum synthesis are shown in the legends. Symbols and lines are the same as in Figure 1.

Table 4Systematic Abundance Uncertainties

Species	Ion	$\Delta T_{ m eff} + 100~{ m K}$	$\Delta \log g$ +0.3 dex	$\Delta v_{\rm micr}$ +0.3 km s ⁻¹	Root Mean Square
<u>C</u>	СН	+0.19	+0.11	0.00	0.27
0	1	+0.22	+0.11	0.00	0.39
Na	1	+0.09	-0.01	-0.02	0.10
Mg	1	+0.09	-0.06	+0.06	0.14
Ca	1	+0.08	-0.01	-0.03	0.12
Sc	2	+0.07	+0.11	-0.02	0.15
Ti	1	+0.10	-0.01	-0.01	0.14
Ti	2	+0.04	+0.08	-0.12	0.16
V	2	+0.05	+0.10	+0.00	0.13
Cr	1	+0.12	-0.01	-0.03	0.15
Mn	1	+0.12	+0.00	-0.01	0.13
Fe	1	+0.12	-0.02	-0.08	0.16
Fe	2	+0.02	+0.11	-0.01	0.14
Co	1	+0.12	0.00	-0.03	0.15
Ni	1	+0.15	-0.03	-0.11	0.20

final derived abundances with those given in Li et al. (2015) was possible. In Figure 3, we compare our [X/Fe] for species in common. Generally, there is good agreement of $-0.20~{\rm dex} < \Delta [{\rm X/Fe}] < +0.20~{\rm dex}$. Still, sodium ($\Delta [{\rm Na/Fe}] = +0.34~{\rm dex}$), strontium ($\Delta [{\rm Sr/Fe}] = -0.34~{\rm dex}$), and samarium ($\Delta [{\rm Sm/Fe}] = -0.40~{\rm dex}$) exhibited larger discrepancies. Taking into account differences in stellar parameters (Li et al. 2015 adopted $T_{\rm eff} = 4440~{\rm K}$, $\log g = 0.70$, $[{\rm Fe/H}] = -3.41$, and $v_{\rm t} = 1.98~{\rm km~s^{-1}}$) somewhat alleviates the discrepancies but cannot fully reconcile them ($\Delta [{\rm Na/Fe}] = +0.25~{\rm dex}$, $\Delta [{\rm Sr/Fe}] = -0.19~{\rm dex}$, and $\Delta [{\rm Sm/Fe}] = -0.35~{\rm dex}$), leaving potential differences in atomic data or measurement technique as a possible explanation.

5. Discussion and Analysis

In this section, we evaluate the chemical enrichment scenario for the natal gas cloud from which J1109+0745 formed. We

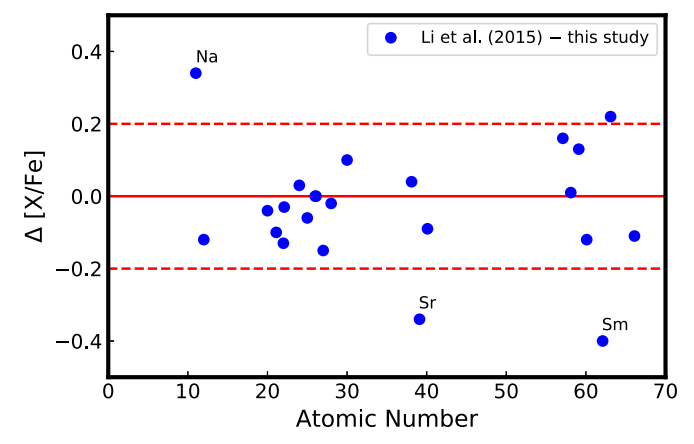


Figure 3. Comparison of our abundances for the elements measured in J1109 \pm 0754 and in common with those presented in Li et al. (2015). The blue filled circles represent differences between abundances calculated as Li et al. (2015) — this work. The solid and dashed lines denote abundance differences of 0 and \pm 0.20 dex, respectively.

were able to measure 31 individual elemental abundances (from lithium to thorium) for J1109+0754. Its neutron-capture elemental abundance pattern indicates that this is an r-II star, following the new definitions for RPE stars ([Eu/Fe] > +0.7 instead of [Eu/Fe] > +1.0 used previously) in Holmbeck et al. (2020), based on new data collected by the RPA. Previously, it would have been considered an r-I star, according to the definitions in Beers & Christlieb (2005). It is thus apparent that the overall abundance signature of J1109+0754 must have arisen after a variety of nucleosynthesis sources, including an r-process event, contributing to the elements we observe today.

5.1. The Light-element Abundance Pattern

J1109+0754 has an approximately solar [C/Fe] ratio. However, based on the $\log g$, it is assumed that J1109+0754 has undergone

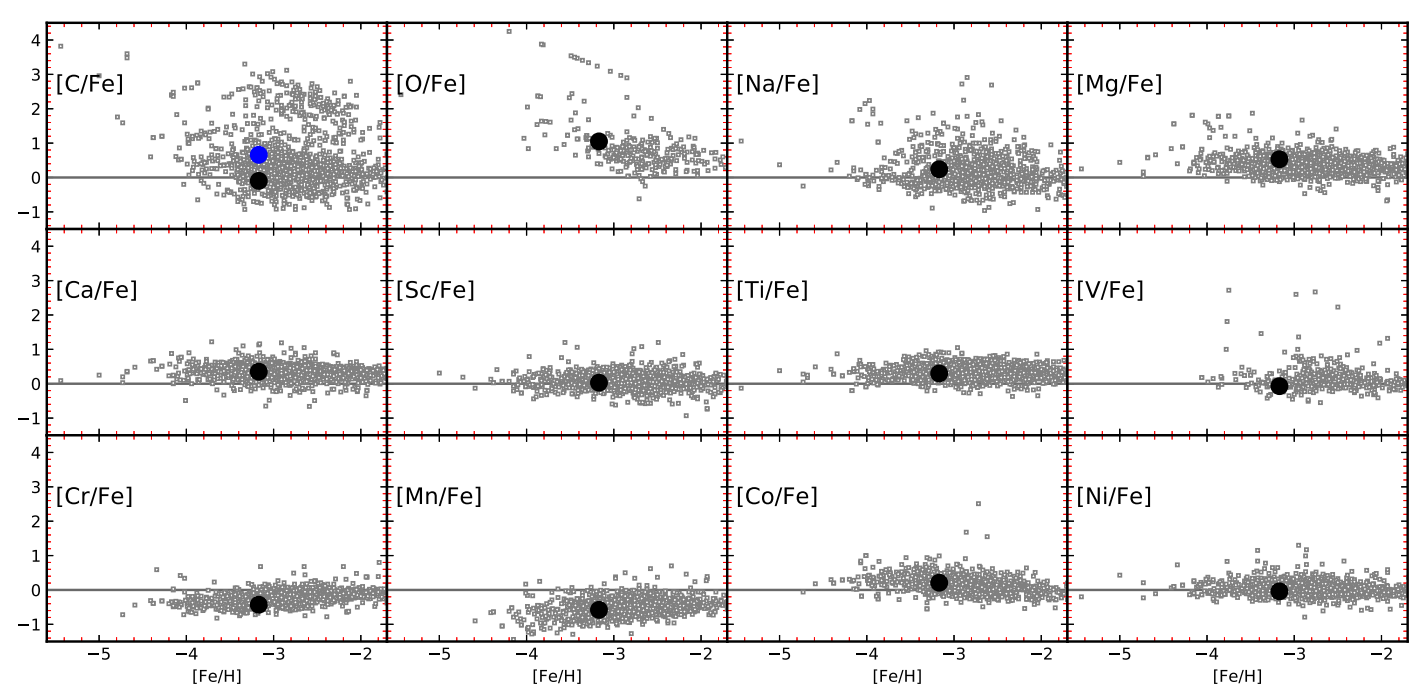


Figure 4. Observed [X/Fe] ratios for elements up to the iron peak, as a function of [Fe/H]. Abundances for J1109+0754 are represented by the large filled black circles, and those of Milky Way field stars with [Fe/H] < 2 are represented by gray squares (JINAbase; Abohalima & Frebel 2018). The filled blue circle denotes the natal carbon abundance of J1109+0745, calculated based on Placco et al. (2014).

carbon depletion, and thus the observed carbon abundance ([C/Fe] = -0.10) does not reflect its natal value. Correcting for this significant effect (Placco et al. 2014) increases the abundance to [C/Fe] = +0.66. Both the measured and corrected C abundances are shown in Figure 4. This suggests that J1109+0754 is close to the regime of strongly carbon-enhanced stars and that significant amounts of carbon were present in its natal gas cloud.

Figure 4 shows the [X/Fe] abundance ratios of the light elements observed in J1109+0754. They all agree well with the abundances of Milky Way field stars taken from JINAbase (Abohalima & Frebel 2018). The observed α -element (Mg, Ca, and Ti) abundances are enhanced with $[\alpha/\text{Fe}] \approx +0.4$, as is typical for metal-poor halo stars.

Due to the extremely low metallicity nature of J1109+0754 ($[Fe/H] = -3.17 \pm 0.09$), we compare the observed light-element abundance pattern with the predicted nucleosynthetic yields of supernovae for high-mass metal-free stars (Heger & Woosley 2010). This allows us to constrain the stellar mass and supernova explosion energy of the progenitor of J1109+0754, assuming that the gas was likely enriched by just one supernova (Mardini et al. 2019b).

Using a normal distribution, we generated 10,000 sets of the observed abundances up to the iron peak from the corresponding measurement errors (σ ; see Table 3), resulting in 10,000 separate abundance patterns. We then used the online STARFIT code to find the best fit for each generated abundance pattern. These theoretical models have wide ranges of stellar mass (10–100 M_{\odot}), explosion energies ((0.3–10) × 10⁵¹ erg), and $f_{\rm mix}$ (no mixing to approximately total mixing).

Figure 5 shows the best fits and their associated information. We found that \approx 93% of the generated patterns match the yields of two models with 22.5 M_{\odot} and explosion energies of 1.8 \times 10⁵¹ erg and 3 \times 10⁵¹ erg. The remainder of the patterns

(\sim 7%) match 30 models with stellar masses ranging from 13.4 to 29.5 M_{\odot} and explosion energies ranging from 0.9×10^{51} erg to 10×10^{51} erg. This agrees with results of Mardini et al. (2019b) and suggests that a single supernova ejecta from a Population III star with 22.5 M_{\odot} can be responsible for the observed light-element pattern of J1109+0754.

It thus appears that J1109+0754 may have formed in a halo that experienced the enrichment by a massive Population III star with a moderate explosion energy.

5.2. The Heavy-element Abundance Pattern

The heavy-element abundances provide key information on the nucleosynthetic sources that operated in the birth environments of metal-poor stars (e.g., formation rates, timescales). Figure 6 (top panel) shows the full *r*-process abundance pattern of J1109+0754, overlaid with the scaled-solar system *r*- and *s*-process components (scaled to Eu and Ba, respectively). The *r*-and *s*-process fractions are adopted from Burris et al. (2000), and isotopic ratios are adopted from Sneden et al. (2008).

The observed heavy-element abundances clearly match the pattern of the main r-process, as evidenced by the small standard deviation of the residuals (observed abundances – scaled-solar r-process pattern). This result supports the universality of the main r-process, as has already been seen for many other metal-poor RPE stars, independent of their metallicity (e.g., Hill et al. 2002; Sneden et al. 2003; Frebel et al. 2007; Roederer et al. 2018; Placco et al. 2020). With [Eu/Fe] = +0.96, J1109+0754 is thus confirmed as an r-II star. In fact, given its enhanced natal carbon abundance ($[C/Fe] = +0.66 \pm 0.27$), J1109+0754 adds to the sample of known CEMP r-II stars.

Deriving abundances of the actinide elements (thorium and uranium) would enable nucleo-chronometric age estimates of J1109+0754. However, only an upper limit for the thorium

²¹ http://starfit.org

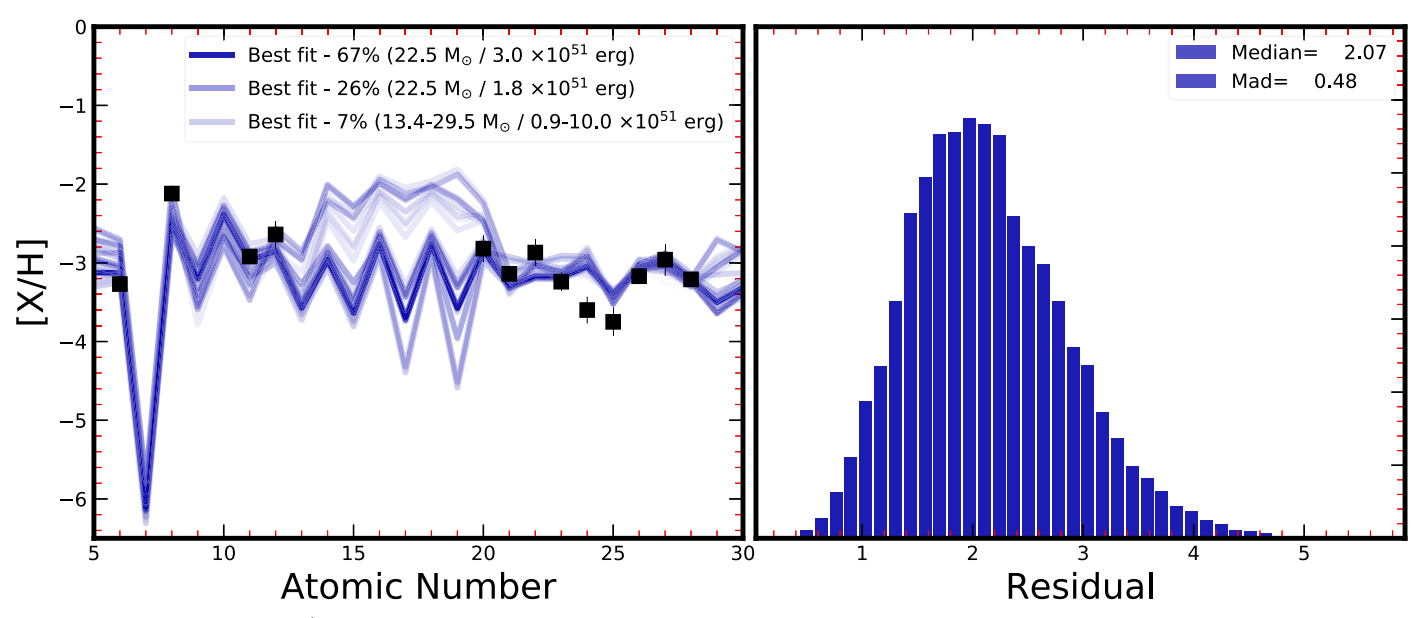


Figure 5. Left panel: observed [X/H] abundance ratios of J1109+0754 (filled black squares), as a function of atomic number, overlaid with the matched predicted nucleosynthetic supernova models. The transparency of the models' lines reflects their fractional appearance. The best fits and their properties are discussed in the text. Right panel: posterior distributions for the mean squared residual, χ^2 , of the 10,000 simulations. The median and median absolute deviation (MAD) are shown in the legend.

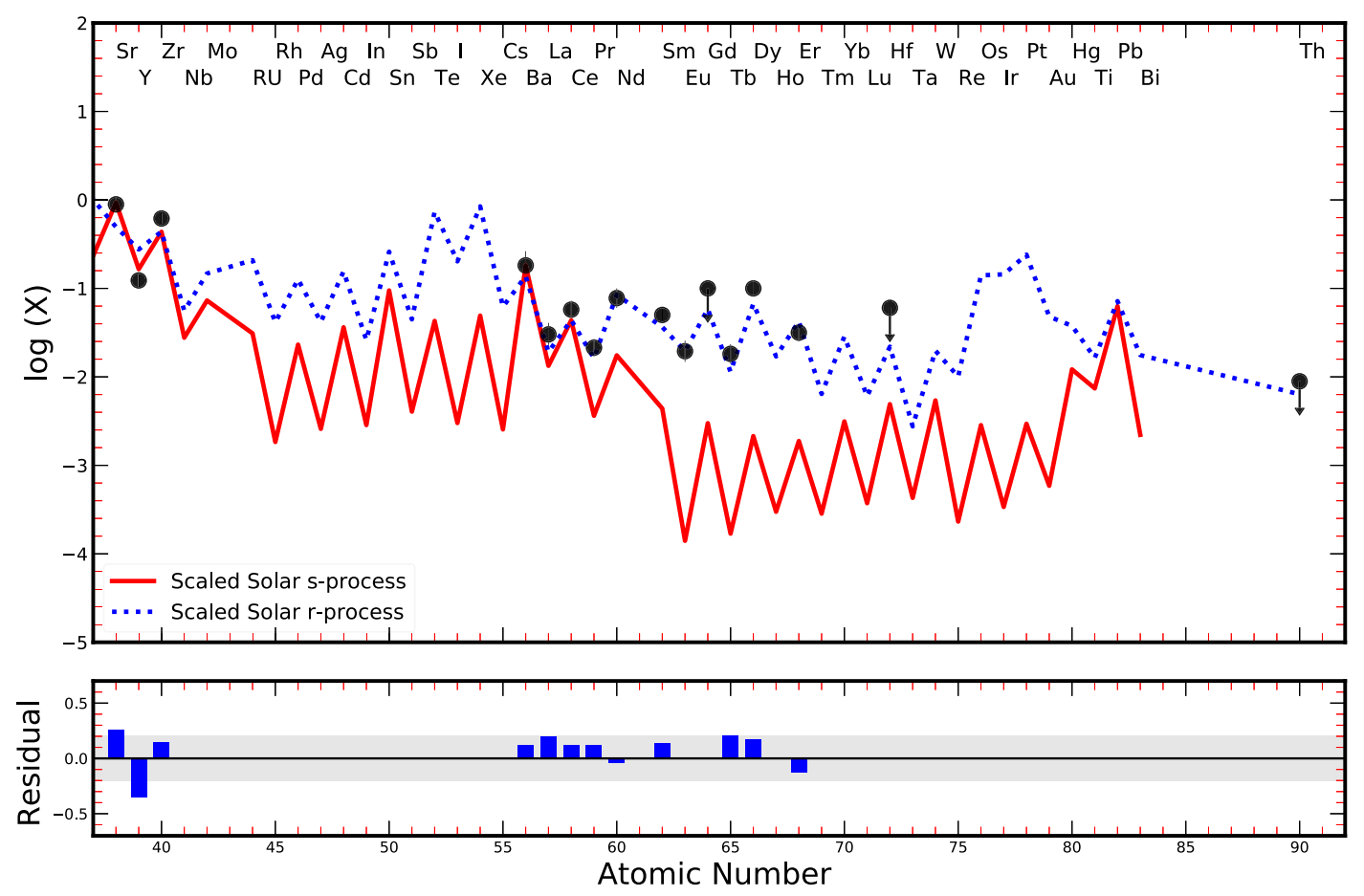


Figure 6. Top panel: heavy-element abundance pattern of J1109+0754 (filled circles), overlaid with the scaled-solar system abundances (SSSA). The solar r- and s-process components (blue and red lines, respectively) are scaled to the observed Eu and Ba, respectively. The r- and s-process fractions are adopted from Burris et al. (2000). Bottom panel: residuals between the observed and the SSSA patterns.

 Table 5

 Positions and Galactic Space-velocity Components

Star	X	Y	Z	U	V	W	V_R	V_{ϕ}	V_{\perp}
		(kpc)			$(km s^{-1})$			$(km s^{-1})$	
J1109+0754	$8.97^{+0.14}_{+0.14}$	$-2.32^{+0.32}_{+0.32}$	$4.22^{+0.28}_{+0.28}$	$-170.12^{+9.3}_{+9.4}$	119.92+13.81	$-133.45^{+7.8}_{+7.6}$	$-194.64^{+16.29}_{+14.55}$	$73.72^{+7.82}_{+8.01}$	235.99+4.31

Note. The - and + indicate the 16th percentile and 84th percentile, respectively.

Table 6Derived Dynamical Parameters

Star	$r_{ m peri}$	r _{apo} (kpc)	$Z_{ m max}$	e	$\frac{E}{(10^3 \text{ km}^2 \text{ s}^{-2})}$	L_z	J_r	J_z (kpc km s ⁻¹)	J_{ϕ}
J1109+0754	$1.88^{+0.89}_{+0.82}$	21.66 ^{+2.90} _{+2.25}	10.87 ^{+1.78} _{+1.83}	$0.84^{+0.08}_{+0.09}$	$-87.05^{+4.12}_{+3.26}$	683.68 ^{+72.95} _{+89.74}	1226.86 ^{+178.21} _{+113.70}	224.04 ^{+5.34} _{+5.89}	683.68 ^{+72.95} _{+89.74}

Note. The - and + indicate the 16th percentile and 84th percentile, respectively.

abundance could be determined, and no uranium features were detected, thus precluding any age measurements.

Finally, we note for completeness that the derived abundances of Sr, Y, and Zr do not match the scaled-solar *r*-process pattern as well. Similar variations have been observed in other RPE stars. The scatter in these abundances likely stems from differences in the yields produced by the limited, or weak, *r*-process (Sneden et al. 1996, 2008; Frebel 2018), or other *r*-process components.

6. Kinematic Signature and Orbital Properties of J1109+0754

The advent of the Gaia mission (Gaia DR2; Gaia Collaboration et al. 2018) has fundamentally changed our view of the nature of the Milky Way. Detailed orbits for many stars can now be obtained from astrometric solutions provided by DR2, which have since led to the discovery of important structures in our Galaxy, e.g., the Gaia–Enceladus–Sausage (Belokurov et al. 2018; Haywood et al. 2018; Helmi et al. 2018; Naidu et al. 2020) and the Sequoia event (Myeong et al. 2019). This followed numerous hints over several decades for the presence of such structures, primarily provided by results from spectroscopy, photometry, and, in some cases, proper motions, using smaller samples of metalpoor stars (e.g., Norris 1986; Sommer-Larsen et al. 1997; Chiba & Beers 2000). The Gaia results identified the reasons for these complexities, validated the previous claims, and gave names to several prominent examples. Other studies (e.g., Carollo et al. 2007, 2010; Beers et al. 2012; An & Beers 2020) then presented evidence for the halo being built by multiple components involving at least an inner- and an outer-halo population.

To investigate the kinematic signature and orbital properties of J1109+0754, we adopted the parallax and proper motion from Gaia Collaboration et al. (2018), the distance from Bailer-Jones et al. (2018), and the RV derived from the APF spectrum as the line-of-sight velocity (see Table 1). We have taken into account the known zero-point offset parallax for bright stars in Gaia DR2, as described in Lindegren et al. (2018).

6.1. Orbital Properties with AGAMA

Unraveling the full kinematic signature of J1109+0754 enables us to learn about its formation history and potentially the environment in which the star formed. Using the public code AGAMA (Vasiliev 2019) with the fixed Galactic potential

MWPotential2014 (see Bovy 2015, for more information), we thus integrate the detailed orbital parameters available for J1109+0754. For that, we generated 10,000 sets of the six-dimensional phase-space coordinates based on the corresponding measurement uncertainties (σ ; see Table 1), to then statistically derive the total orbital energy and calculate the three-dimensional action ($J = (J_r, J_\phi, J_z)$). We also calculate Galactocentric Cartesian coordinates ($X_{\rm GC}$, $Y_{\rm GC}$, $Z_{\rm GC}$), Galactic space-velocity components (U, V, W), and cylindrical velocity components (V_R , V_ϕ , V_z), which are defined in the same way as presented in Mardini et al. (2019a, 2019b).

For our calculations, we assume that the Sun is located on the Galactic midplane $(Z_{\odot}=0)$ at a distance of $R_{\odot}=8.0$ kpc from the Galactic center (Foster & Cooper 2010). The local standard of rest (LSR) velocity at the solar position is $v_{\rm LSR}=232.8$ km s⁻¹ (McMillan 2017), and the motion of the Sun with respect to the LSR is $(U_{\odot},V_{\odot},W_{\odot})=(11.1,12.24,7.25)$ km s⁻¹ (Schönrich et al. 2010). We define the total orbital energy as $E=(1/2)v^2+\Phi(x)$, the eccentricity as $e=(r_{\rm apo}-r_{\rm peri})/(r_{\rm apo}+r_{\rm peri})$, the radial and vertical actions $(J_r$ and J_z , respectively) to be positive (see Binney 2012, for more information), and the azimuthal action by

$$J_{\phi} = \frac{1}{2\pi} \oint_{\text{orbit}} d\phi \ RV_{\phi} = -L_{z}. \tag{1}$$

Table 5 lists the calculated median for the Galactic positions and Galactic velocities. Table 6 lists the medians for the orbital energy, orbital parameters, and the three-dimensional actions. The sub- and superscripts denote the 16th and 84th percentile confidence intervals, respectively, for each of these quantities.

These results show that J1109+0754 possesses a bounded (E < 0), nonplanar $(J_z \neq 0 \text{ and } Z_{\text{max}} \neq 0)$, and eccentric $(J_r \neq 0 \text{ and } e \neq 0)$ orbit. Moreover, the positive J_ϕ and V_ϕ values (see Table 5) indicate that J1109+0754 is on a prograde orbit. Figure 7 shows the last 10 orbital periods of J1109+0754, in different projections (XY, XZ, and YZ) onto the Galactic plane, integrated for 4.2 Gyr. The minimum distance of J1109+0754 from the center (pericenter = $1.9^{0.9}_{0.8}$ kpc), the maximum distance (apocenter = $21.7^{2.9}_{2.3}$ kpc), and the maximum height of the star above the Galactic plane $(Z_{\text{max}} = 10.9^{1.8}_{1.8} \text{ kpc})$) suggest that the orbit of our star reaches out to distances of the inner-/outer-halo overlap region.

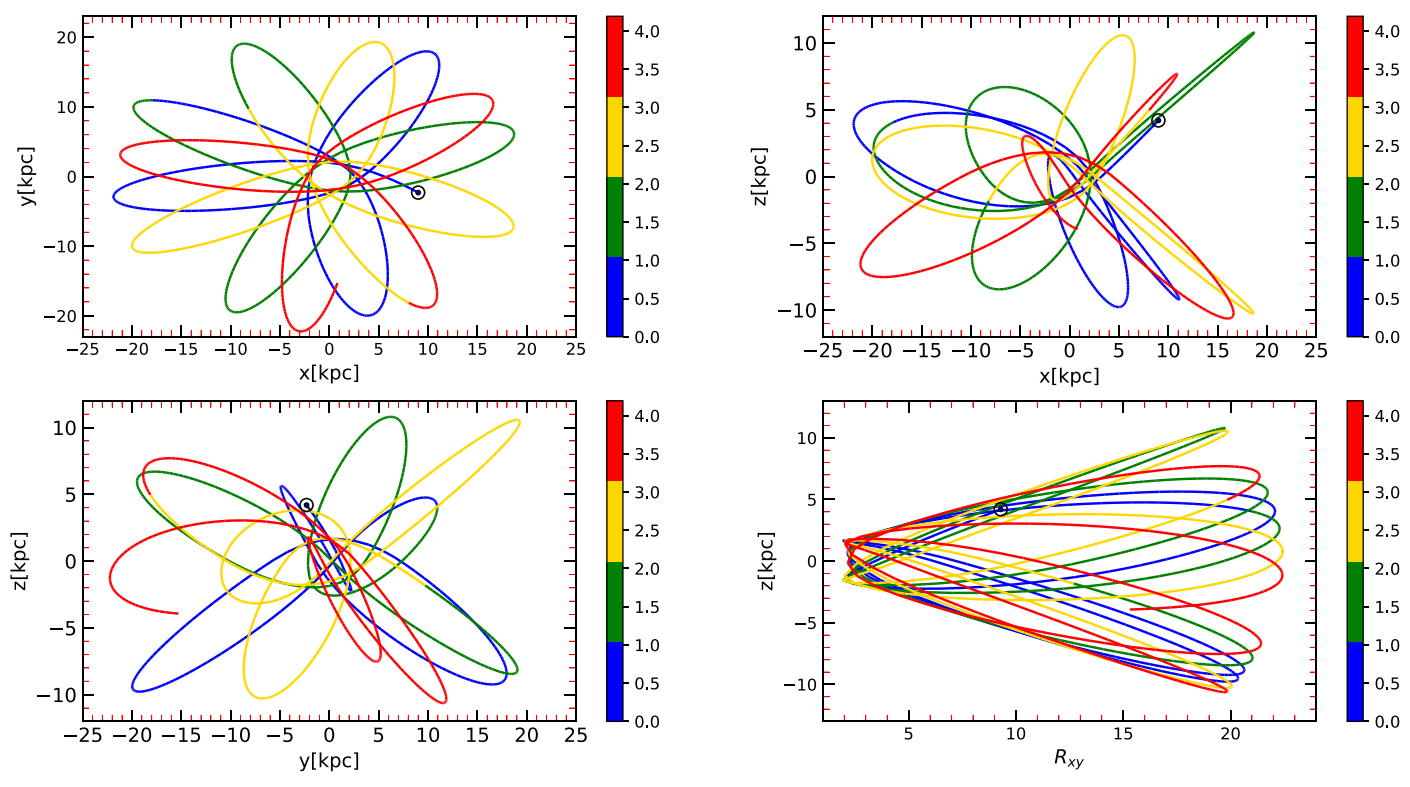


Figure 7. Orbits of J1109+0754, integrated in time for 4 Gyr in the Galactic potential MWPotential2014. The top panels show $Y_{\rm GC}$ (left) and $Z_{\rm GC}$ (right), as a function of $X_{\rm GC}$. The bottom panels show $Z_{\rm GC}$ as a function of $Y_{\rm GC}$ (left) and Galactocentric radius, R_{xy} (right). The black points in all panels indicate the current location of J1109+0754.

6.2. Detailed Kinematic History of J1109+0754

The kinematic results from Section 6.1 are insightful, but limited, given that fixed Galactic potential has been used. Below we explore a novel approach with the goal of obtaining a less idealized and more realistic time-dependent kinematic history of J1109+0754 within the Milky Way halo, which itself was built from smaller accreted dwarf galaxies, one of which likely contributed this star to the halo at early times.

In order to do so, we combine our custom high-order Hermite4 code φ –GRAPE (Harfst et al. 2007). It uses a GPU/CUDA-based GRAPE emulation YEBISU library (Nitadori & Makino 2008). It has been well tested and used with several large-scale (up to a few million particles) simulations (Just et al. 2012; Li et al. 2012; Wang et al. 2014; Zhong et al. 2014; Kennedy et al. 2016; Meiron et al. 2020). We selected the particle data of Milky Way analogs from the publicly available Illustris-TNG cosmological simulation set (Rodriguez-Gomez et al. 2015; Marinacci et al. 2018; Naiman et al. 2018; Nelson et al. 2018, 2019a, 2019b; Pillepich et al. 2018, 2019; Springel et al. 2018). Our goal is to establish a *time-varying* potential, based on the subhalo's snapshot data for all redshifts, and then carry out a detailed integration of J1109+0754's orbital parameters over some 10 Gyr backward in time.

6.2.1. Selecting Milky Way-like Galaxies in Illustris-TNG

We use the Illustris-TNG TNG100 simulation box, characterized by a length of \sim 110 Mpc. TNG100 is the second-highest-resolution simulation box among the TNG simulations

and has the highest resolution of the publicly available data. The TNG100 simulation box is thus sufficiently large to contain many resolved Milky Way–like disk galaxies. The mass resolution in TNG100 is $7.5 \times 10^6\,M_\odot$ and $1.4 \times 10^6\,M_\odot$ for dark matter and baryonic particles, respectively. This resolution is larger, by a factor of \sim 10, than the corresponding mass resolution of particles in TNG300, allowing a more accurate description of structure formation and evolution. Given that Milky Way–like galaxies have dark matter halos of $\sim 10^{12}\,M_\odot$ and disks with $\sim 10^{10}\,M_\odot$, we identify simulated galaxy candidates, with 10^5-10^6 dark matter particles and 10^3-10^4 stellar particles, to ensure good particle-number statistics.

To select potential Milky Way analogs, we target all z=0 galaxies (subhalos) that reside in the centers of massive halos with $0.6 \times 10^{12} < M_{200}/M_{\odot} < 2 \times 10^{12}$ (where M_{200} is defined as the total halo mass in a sphere whose density is 200 times the critical density of the universe; Navarro et al. 1995). This mass range reflects literature values (e.g., Grand et al. 2017; Buck et al. 2020) and corresponds to stellar masses in accordance with observations (McMillan 2011).

We then pared down an initial list of over 2000 candidates using the following criteria: (i) Stellar subhalo mass: we enforce a 3σ range of the Milky Way stellar mass (Calore et al. 2015), by only counting galaxies with a total stellar mass of $4.5 \times 10^{10} M_{\odot} < M < 8.3 \times 10^{10} M_{\odot}$. (ii) Morphology: to account for the disky structure of the Milky Way, we select only galaxies with a triaxiality parameter T < 0.35, which we define as $T = \sqrt{(c/a)^2 + (1 - (b/a))^2}$, where a, b, and c are the principal axes of inertia. (iii) Kinematics: to select disky galaxies, we also calculate the circularity parameter of each stellar particle, $\epsilon = j_z/j$, where j_z is the specific angular momentum along the z-axis and j is the total specific angular momentum of the star (Abadi et al. 2003).

 $[\]overline{^{22}}$ The current version of the φ -GRAPE code is available at ftp://ftp.mao.kiev.ua/pub/berczik/phi-GRAPE/.

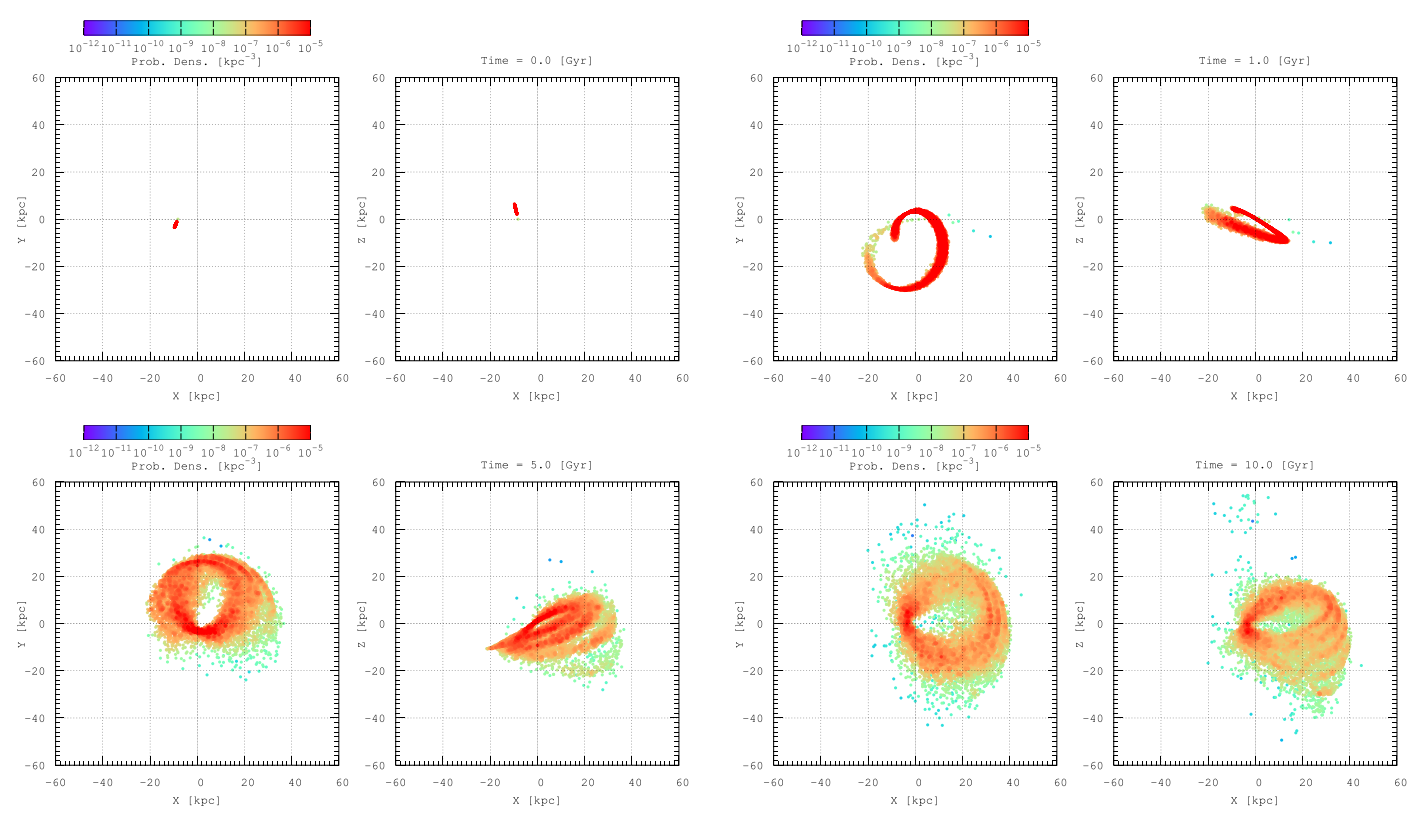


Figure 8. Results of the backward integration (for 10 Gyr) of LAMOST J1109+0754's orbital parameters following 10,000 random coordinates and velocity realizations (inside $\pm 2\sigma$) for Illustris-TNG halo #489100. The color-coding captures the probability number density of the orbits in a 1 kpc³ cube at each point.

Only galaxies that have at least 40% of stars with $\epsilon > 0.7$ (Marinacci et al. 2014) are counted. (iv) Disk-to-total mass ratio: we only select galaxies with stellar populations with disk-to-total mass ratios between 0.7 and 1, corresponding to the Milky Way's ratio of 0.86 (McMillan 2011). Stars with $\epsilon > 0.6$ are assigned to the disk.

By applying the above criteria, we obtain a total of 123 Milky Way-like candidates. We emphasize that the goal of our study is not to test the capability of TNG100 to reproduce Milky Way-like galaxies. Therefore, we acknowledge that these criteria, while sufficient for our work, do not necessarily reflect the true number of Milky Way analogs in TNG100. Unfortunately, not all of these subhalos are equally useful for establishing a time-dependent potential: If parameters change too much between consecutive snapshots, the resulting interpolation is not accurate enough. This typically occurs as a result of the subhalo switching problem (see description in Poole et al. 2017), where a group of loosely bound particles is included in one of our subhalos in some snapshots (by the Subfind algorithm) but excluded in others. We finally chose five subhalos as the most suitable Milky Way analogs for our study, and we use their corresponding potentials for our orbital integrations.

6.2.2. Establishing the ORIENT

To obtain a time-varying potential for each Galactic analog, we model the gas and dark matter particles as a single Navarro–Frenk–White (NFW; Navarro et al. 1995) sphere and the stellar particles as a Miyamoto & Nagai (1975) disk. The best-fitting parameters are found for each snapshot using a smoothing spline fitting procedure (see Appendix A). The complete potential for each subhalo across all snapshots is then a set of parameters for the disk and the stellar halo as obtained from each TNG100

snapshot. To obtain the gravitational force as a function of time, we interpolate between each snapshot's parameters. Effectively, all the individual integrations for each snapshot are *not* one true *N*-body simulation, but a series of independent one-body simulations or scattering experiments (i.e., test-particle integration in a external potential). To efficiently perform these experiments with 10,000 particles at once, we take advantage of the parallel framework of the φ -GRAPE code.

To find the optimal integration parameter, η , which drives the integration accuracy of our code, we first ran short (up to 1 Gyr) test simulations with different values of η (0.020, 0.010, 0.005, 0.001) using a Milky Way fixed model, taken from Ernst et al. (2011; see also their Figure 1). Using $\eta = 0.01$ limits the total relative energy drift $(dE_{\rm tot}/E_{\rm tot}(t=0))$ in a 10 Gyr forward integration in the fixed Milky Way potential to below $\approx 2.5 \times 10^{-13}$, thus optimizing code speed versus accuracy.

6.2.3. Results

Figure 8 shows the results of the backward orbital integrations of the 10,000 realizations in our selected <code>Illustris-TNG</code> subhalo #489100. It is clear that after $\sim 1\,\mathrm{Gyr}$, the initial positions of the random cloud extend over the entire model galaxy range. The color-coding in the figure shows the probability number density of the orbits in a 1 kpc³ cube at each point. After 10 Gyr of backward integration, the positions of some realizations extend up to $\sim 60\,\mathrm{kpc}$ from the center. This implies that they are already a part of the outer halo of our simulated galaxy. This finding supports the likely external origin (larger galaxy merger or smaller dwarf tidal disruption) of J1109+0754.

Figure 9 shows the backward orbits of a J1109+0754-like star, using the realizations that extend very far from the center, inside our selected subhalo #489100. The integration is

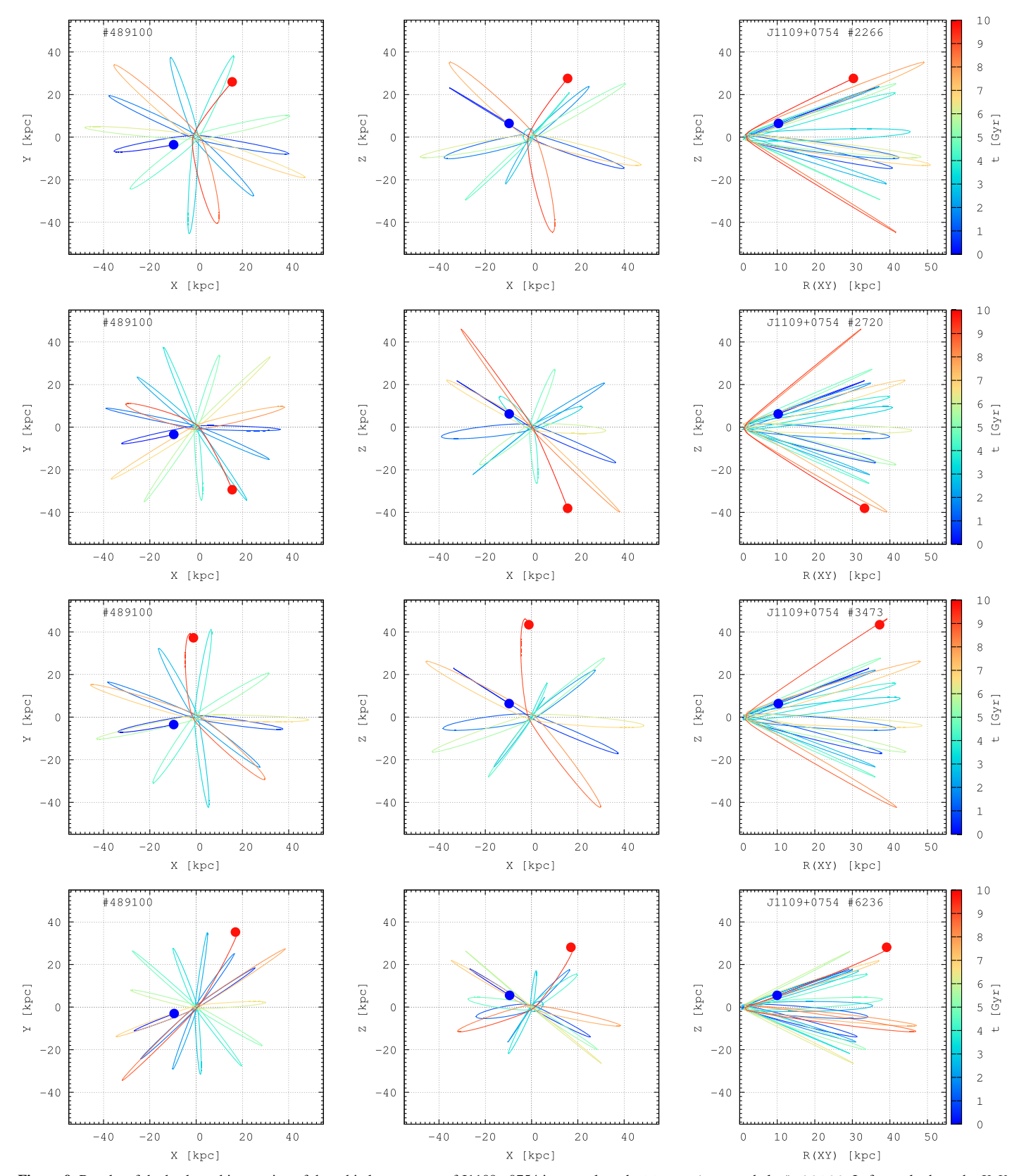


Figure 9. Results of the backward integration of the orbital parameters of J1109+0754 in our selected Illustris-TNG halo #489100. Left panels show the X-Y coordinates of the orbits, middle panels present the X-Z coordinates, and the right panels show the time evolution in cylindrical coordinates R(XY)-Z. The color-coding corresponds to the time from 0 (i.e., the present) to 10 Gyr backward in time. Rows show different random realizations: #2266, #2720, #3473, #6236 (inside $\pm 2\sigma$ from the initial 10,000 random values) of our star's initial positions and velocities.

performed in a backward fashion, from present day to a lookback time of 10 Gyr. The orbits in Figure 7, which are the result of a similar backward integration, but in a static potential, exhibit a more regular behavior, with the $r_{\rm apo}$ and $r_{\rm peri}$ distances being similar in different epochs. The difference between Figure 9 and Figure 7 is particularly evident with our integration using subhalo #489100. As can be seen from Figure 9, the $r_{\rm apo}$ at early cosmic time is significantly larger than at present. Moreover, in some of the models, J1109+0754 enters the outer-halo region (up to \sim 60 kpc) after \sim 6–7 Gyr. These orbits thus suggest a possible external origin of J1109+0754.

Collectively, the peculiar abundance pattern and the results from the backward orbital integrations of J1109+0754 suggest that it was formed in a low-mass dwarf galaxy located \sim 60 kpc from the center of the Galaxy and accreted \sim 6–7 Gyr ago.

7. Conclusions

In this study, we present a detailed chemodynamical analysis of the extremely metal-poor star LAMOST J1109+0754. The available RV measurements for this relatively bright (V=12.8) star suggest that J1109+0754 is not in a binary system, and thus its abundance pattern is not likely due to mass transfer from an unseen evolved companion; this is consistent with its observed subsolar carbon abundance ([C/Fe] = -0.10; natal abundance [C/Fe] = +0.66). In addition, J1109 +0754 exhibits enhancements in the α -elements ([α /Fe] \approx +0.4) and large enhancements in the r-process elements ([Ba/Fe] = $+0.25\pm0.21$ and [Eu/Fe]= $= +0.94\pm0.12$), indicating that J1109+0754 is a CEMP r-II star, with no evidence of s-process contribution ([Ba/Eu] = -0.69).

The observed light-element abundances do not deviate from the general trend observed for other metal-poor field stars reported in the literature. Moreover, the comparison between these abundances and the predicted yields of high-mass metal-free stars suggests a possible Population III progenitor with stellar mass of $22.5~M_{\odot}$ and explosion energies of $1.8-3.0~10^{51}$ erg. The fitting result of this exercise supports the conclusion presented in Mardini et al. (2019b), which suggests that a stellar mass $\sim 20~M_{\odot}$ progenitor may reflect the initial mass function of the first stars. Furthermore, it raises the question as to whether more massive supernovae might be more energetic, and therefore destroy their host halo and not allow for EMP star formation afterward.

The observed deviations of Sr, Y, and Zr from the scaled-solar r-process pattern indicate that the production of these elements (in the first r-process peak) is likely to be different from the second and third r-process peaks; these deviations are observed in other RPE stars. The universality of the main r-process is confirmed for LAMOST J1109+0754 as well, due to the good agreement between the abundances of the elements with Z > 56 and the scaled-solar r-process residuals.

To carry out a detailed study of the possible orbital evolution of LAMOST J1109+0754, we carefully selected Milky Way-like galaxies from the Illustris-TNG simulation. We modeled the ORIENT from each candidate to be able to integrate the star's backward orbits. The results show that, in most cases, the star presents an extended Galactic orbit around 10 Gyr ago (up to 60 kpc, well into the outer-halo region) but is still bound to the Galaxy. These results, however, do not exclude the possibility that J1109+0754 has been accreted, as they are consistent with it being part of a dissolving dwarf

galaxy positioned at about ${\sim}60\,\mathrm{kpc}$ from the center of the Galaxy ${\sim}6{-}7\,\mathrm{Gyr}$ ago. One caveat in our method to reconstruct the orbit is our selection criteria for Milky Way analog subhalos, specifically discarding those that exhibited "noisy" behavior, which may have biased the integration results toward orbits that remain bound. Another caveat is that backward integration may not be an ideal tool to establish the true phase-space coordinates of a star in the distant past, given the obvious limitations of the models for the gravitational potential at the very earliest times.

In future work, we plan to increase the number of Milky Way analog subhalos and perform forward integration using initial conditions generated from the spatial and velocity distributions of particles in these subhalos. This will allow us to quantify the probability that LAMOST J1109+0754 has been accreted into the Milky Way and to answer questions such as when this accretion event may have occurred and what was the likely mass of its progenitor subhalo.

We thank the anonymous referee for positive remarks that helped us to improve this manuscript. M.K.M. thanks Ian Roederer and Tilman Hartwig for valuable discussions and helpful comments on earlier versions of the manuscript. This work was supported by the National Natural Science Foundation of China under grant Nos. 11988101 and 11890694 and National Key R&D Program of China No. 2019YFA0405502. V.M.P., T.C.B., and A. F. acknowledge partial support for this work from grant PHY 14-30152, Physics Frontier Center/JINA Center for the Evolution of the Elements (JINA-CEE), awarded by the US National Science Foundation. A.F. acknowledges support from NSF grant AST-1716251. M.A.S. acknowledges financial support from the Alexander von Humboldt Foundation under the research program "Black holes at all the scale." M.A.S., M.D., and M.M. acknowledge financial support by the Deutsche Forschungsgemeinschaft (DFG, German Research Foundation)-Project-ID 138713538—SFB 881 ("The Milky Way System," sub-projects A01, A02). M.A.S., B.A., and M.M. are grateful to Dylan Nelson, who helped in transferring the TNG data set used in this work. The work of P.B. and M.I. was supported by the Deutsche Forschungsgemeinschaft (DFG, German Research Foundation) Project-ID 138713538, SFB 881 ("The Milky Way System"), and by the Volkswagen Foundation under the Trilateral Partnerships grant No. 97778. P.B. acknowledges support by the Chinese Academy of Sciences (CAS) through the Silk Road Project at NAOC, the Presidents International Fellowship (PIFI) for Visiting Scientists program of CAS, and the National Science Foundation of China (NSFC) under grant No. 11673032. M.I. acknowledges support by the National Academy of Sciences of Ukraine under the Young Scientists grant No. 0119U102399. The work of P.B. was also partially supported under the special program of the National Academy of Sciences of Ukraine "Support for the development of priority fields of scientific research" (CPCEL 6541230). The work of B.A. was funded by a "Landesgraduiertenstipendium" of the University of Heidelberg and the Trilateral Collaboration Scheme project "Accretion Processes in Galactic Nuclei." This work has made use of data from the European Space Agency (ESA) mission Gaia (https://www.cosmos.esa.int/gaia), processed by the Gaia Data Processing and Analysis Consortium (DPAC, https://www. cosmos.esa.int/web/gaia/dpac/consortium). Funding for the DPAC has been provided by national institutions, in particular the institutions participating in the Gaia Multilateral Agreement.

Facilities: APF, Gaia, Gauss: HLRS (Illustrius-TNG).

Software: Astropy (Astropy Collaboration et al. 2013, 2018), linemake (https://github.com/vmplacco/linemake), IRAF (Tody 1986, 1993), Matplotlib (Hunter 2007), MOOG (Sneden 1973; Sobeck et al. 2011), NumPy (van der Walt et al. 2011), φ -GRAPE (Harfst et al. 2007), SciPy (Virtanen et al. 2020), STARFIT (Heger & Woosley 2010), TAME (Kang & Lee 2015).

Appendix A Parameter Fitting of the Milky Way Analogs

The bottom panels of Figure 10 show the extracted intrinsic parameters of the disk, as a function of the look-back time (red symbols) and the smoothing spline (blue dashed curve), respectively. The disk has three intrinsic parameters: length scales a and b, and mass $M_{\rm d}$. It additionally has a direction

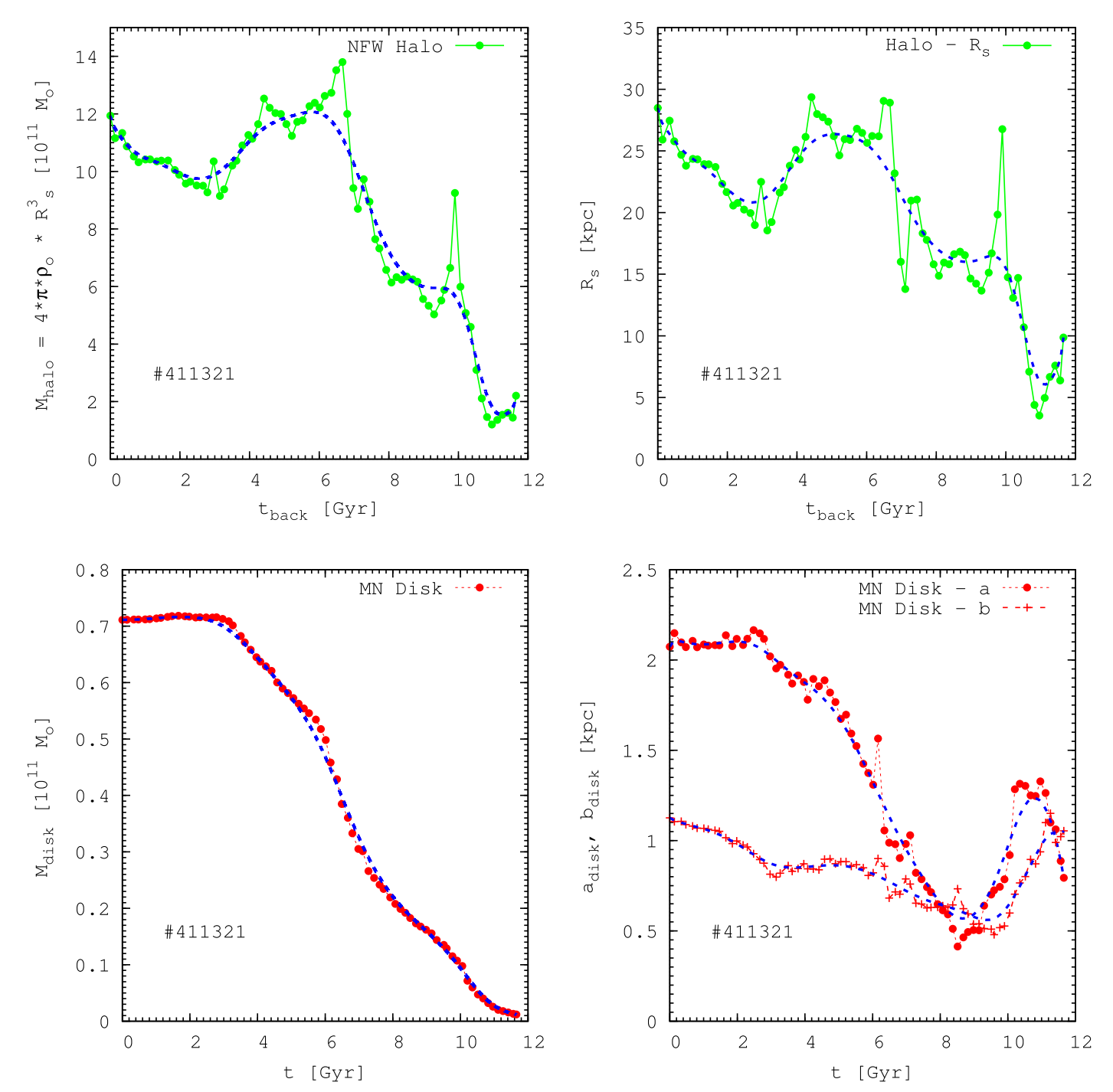


Figure 10. Time evolution of subhalo #411321. Halo and disk total masses are provided in units of $10^{11} M_{\odot}$. The time axis is the look-back time in Gyr. We also present the NFW halo scale radius, R_s (in kpc units), and time evolution, together with the Miyamoto-Nagai disk scale parameters a and b (in kpc units). The points represent the direct data from the Illustris-TNG values (red or green points connected with red or green dashed lines). The dashed blue lines are the Bézier curve smooth data. For smoothing, we use 12,000 equally time-spaced data points.

vector and a center that needs to be calculated as well. Note that we did not include any bulge component, as including it did not significantly improve the fitting of each snapshot.

The fitting procedure starts by searching for the density center of the stellar particles by recursively calculating the center of mass and removing star particles that lie outside of a predefined search radius. Then, the orientation of the disk is found by calculating the eigenvalues and eigenvectors of the quadrupole tensor of the particle distribution with respect to the density center. The largest eigenvalue corresponds to the shortest axis and thus the orientation of the disk. As a consistency check, we also calculate the angular momentum of particles within the distribution's half-mass radius. We find that they agree very well (up to a sign because clockwise and counterclockwise disks have the same quadrupole tensor) except for some snapshots, usually at high redshift, when no clear disk is formed, and the stellar particle's distribution is rather spherically symmetric.

The disk's mass is simply the sum of the stellar particle masses. The disk's length scales are calculated from the medians of the cylindrical radius and z coordinates. The ratio between these medians is mapped to the ratio b/a of the Miyamoto–Nagai disk model using a lookup table, and the scaling could be determined by either median (we use the average of both). This method yields more robust results than a least-squares fitting of the density field of the particle distribution. Using the least-squares method often results in multiple solutions to a and b, depending on the initial guesses. This numerical problem is a result of the stellar distribution not actually following a Miyamoto–Nagai disk model very closely. By considering the median values, outliers have a smaller effect.

Each halo has two intrinsic parameters: central density, ρ_0 , and length scale, a. It additionally has a center that is calculated the same way as the disk's, but using the gas and dark matter particle distributions. The intrinsic parameters are calculated using a least-squares method, where the square differences between the cumulative mass from the center and that of the NFW model are minimized. The top panels of Figure 10 show the extracted intrinsic parameters of the halo as a function of

the look-back time (green symbols) and the smoothing spline fitting function (blue dashed curve).

We find that the offset between the disk and stellar halo centers did not exceed ~ 1 kpc. This is typically much smaller than the stellar halo's length scale. Therefore, the calculations were done in a coordinate system centered at the density center of the disk component. The direction of the coordinate system was chosen in such a way that the disk pointed toward the positive *z*-direction in the last snapshot (representing the present day).

Appendix B Selected Halo Properties

Figure 10 denotes the mass- and size-parameter time evolution of one of our selected halos, #411321.²³ The NFW halo and the Miyamoto-Nagai disk total-mass time evolution in the units of $10^{11} M_{\odot}$ are presented. The time axis corresponds to the look-back time in Gyr. We also present the NFW halo scale radius, R_s (in kpc units), and time evolution, together with the Miyamoto–Nagai disk scale parameters a and b (in kpc units). The connected points represent the direct Illustris-TNG values. For the real calculations, we smooth the data using the Bézier curve smoothing algorithm in the gnuplot software package. These fitted and smoothed curves (dashed lines) have one point for every 1 Myr of time evolution. Integration time steps could be significantly smaller than that, but the curves are smooth enough for simple linear interpolation between these points with sufficient accuracy. A high frequency is necessary in order to achieve a smooth integration of our stellar orbits in this time-dependent and complex external potential field.

Figure 11 presents the time evolution of the circular rotational velocity at the location of the Sun ($R_{XY} = 8 \text{ kpc}$, Z = 0) for the selected subhalos (#441327, #462077, #451323, #474170). To obtain this value, we calculate for each time the enclosed total halo and disk mass inside the solar cylinder. These curves show, in principle, the level of accuracy of our Milky Way approximation with these halos. It is clear that our selected Illustris-TNG halos agree reasonably well with the present-day solar neighborhood rotation.

 $[\]overline{^{23}}$ The number corresponds to the SubfindID at redshift z = 0 in TNG100.

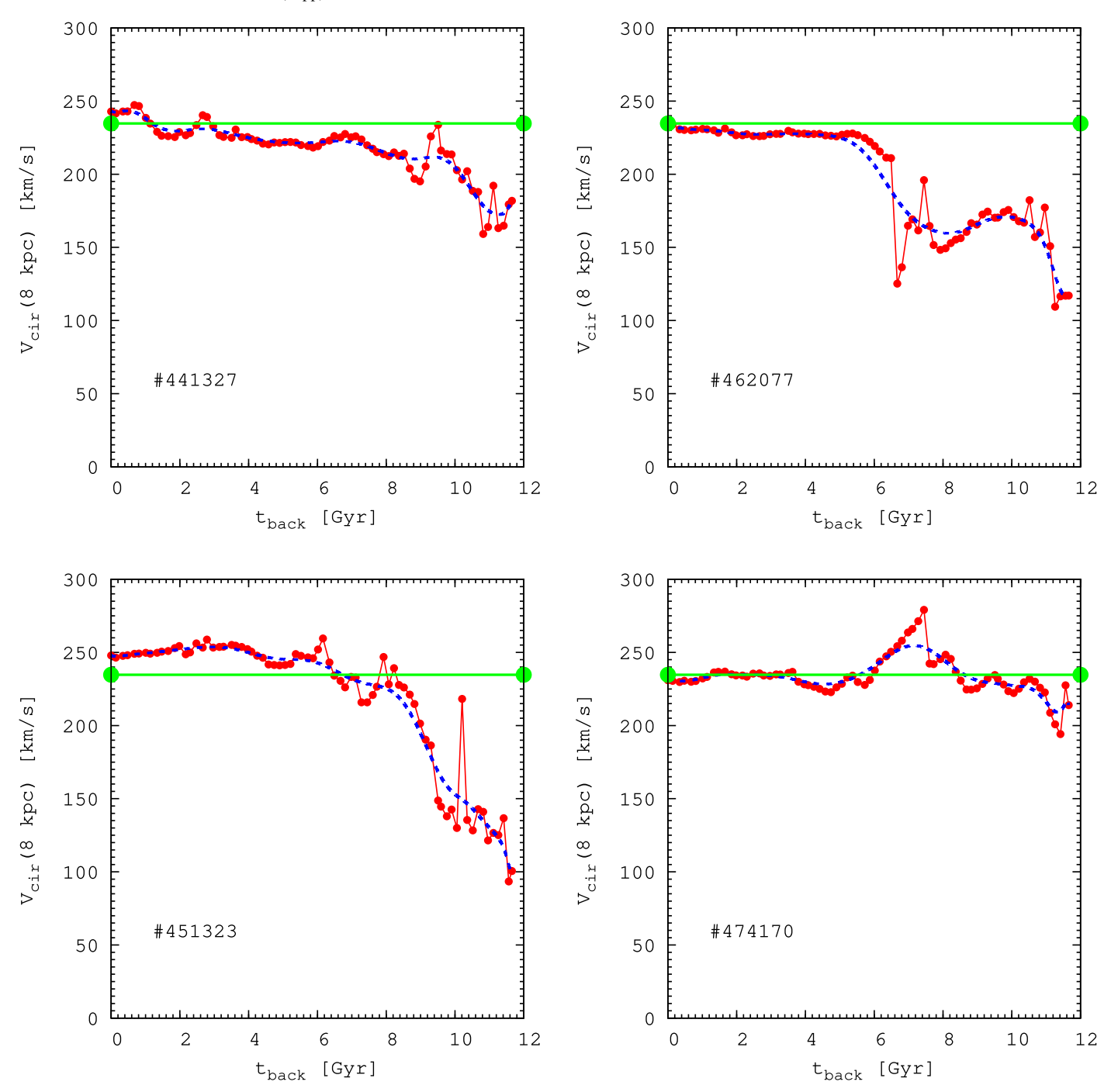


Figure 11. Time evolution of the model circular rotational velocity at the location of the Sun ($R_{XY} = 8$ kpc, Z = 0) for selected subhalos #441327, #462077, #451323, and #474170 (from left to right and from top to bottom). The horizontal lines (green) show our currently adopted circular velocity at the Sun's location of 234 km s⁻¹. The lines with red points show the actual data points from Illustris-TNG. The dashed blue lines show the smoothed data points.

ORCID iDs

Mohammad K. Mardini https://orcid.org/0000-0001-9178-3992

Vinicius M. Placco https://orcid.org/0000-0003-4479-1265
Yohai Meiron https://orcid.org/0000-0003-3518-5183
Marina Ishchenko https://orcid.org/0000-0002-6961-8170
Branislav Avramov https://orcid.org/0000-0002-1638-3080
Matteo Mazzarini https://orcid.org/0000-0002-9293-821X
Peter Berczik https://orcid.org/0000-0003-4176-152X
Manuel Arca Sedda https://orcid.org/0000-0002-3987-0519
Timothy C. Beers https://orcid.org/0000-0003-4573-6233

Anna Frebel https://orcid.org/0000-0002-2139-7145
Ali Taani https://orcid.org/0000-0002-1558-1472
Martina Donnari https://orcid.org/0000-0001-8903-7026
Mashhoor A. Al-Wardat https://orcid.org/0000-0002-0263-9014

Gang Zhao https://orcid.org/0000-0002-8980-945X

References

Abadi, M. G., Navarro, J. F., Steinmetz, M., & Eke, V. R. 2003, ApJ, 597, 21 Abbott, B. P., Abbott, R., Abbott, T. D., et al. 2017a, ApJL, 848, L12 Abbott, B. P., Abbott, R., Abbott, T. D., et al. 2017b, PhRvL, 119, 161101

```
Abohalima, A., & Frebel, A. 2018, ApJS, 238, 36
Alonso, A., Arribas, S., & Martínez-Roger, C. 1999, A&AS, 140, 261
An, D., & Beers, T. C. 2020, ApJ, 897, 39
Asplund, M., Grevesse, N., Sauval, A. J., & Scott, P. 2009, ARA&A, 47, 481
Astropy Collaboration, Price-Whelan, A. M., Sipőcz, B. M., et al. 2018, AJ,
   156, 123
Astropy Collaboration, Robitaille, T. P., Tollerud, E. J., et al. 2013, A&A,
   558, A33
Bailer-Jones, C. A. L., Rybizki, J., Fouesneau, M., Mantelet, G., & Andrae, R.
   2018, AJ, 156, 58
Barklem, P. S., Christlieb, N., Beers, T. C., et al. 2005, A&A, 439, 129
Beers, T. C., Carollo, D., Ivezić, Ž, et al. 2012, ApJ, 746, 34
Beers, T. C., & Christlieb, N. 2005, ARA&A, 43, 531
Belokurov, V., Erkal, D., Evans, N. W., Koposov, S. E., & Deason, A. J. 2018,
   MNRAS, 478, 611
Binney, J. 2012, MNRAS, 426, 1324
Bovy, J. 2015, ApJS, 216, 29
Brauer, K., Ji, A. P., Frebel, A., et al. 2019, ApJ, 871, 247
Buck, T., Obreja, A., Macciò, A. V., et al. 2020, MNRAS, 491, 3461
Burbidge, E. M., Burbidge, G. R., Fowler, W. A., & Hoyle, F. 1957, RvMP,
   29, 547
Burris, D. L., Pilachowski, C. A., Armandroff, T. E., et al. 2000, ApJ, 544, 302
Calore, F., Bozorgnia, N., Lovell, M., et al. 2015, JCAP, 2015, 053
Cameron, A. G. W. 1957, PASP, 69, 201
Carollo, D., Beers, T. C., Chiba, M., et al. 2010, ApJ, 712, 692
Carollo, D., Beers, T. C., Lee, Y. S., et al. 2007, Natur, 450, 1020
Castelli, F., & Kurucz, R. L. 2003, in IAU Symp. 210, Modelling of Stellar
   Atmospheres, ed. N. Piskunov, W. W. Weiss, & D. F. Gray (San Francisco,
   CA: ASP), A20
Charbonnel, C. 1995, ApJL, 453, L41
Chiba, M., & Beers, T. C. 2000, AJ, 119, 2843
Christlieb, N., Beers, T. C., Barklem, P. S., et al. 2004, A&A, 428, 1027
Côté, B., Belczynski, K., Fryer, C. L., et al. 2017, ApJ, 836, 230
Côté, B., Eichler, M., Arcones, A., et al. 2019, ApJ, 875, 106
Cowan, J. J., Cameron, A. G. W., & Truran, J. W. 1983, ApJ, 265, 429
Cowperthwaite, P. S., Berger, E., Villar, V. A., et al. 2017, ApJL, 848, L17
Cui, X.-Q., Zhao, Y.-H., Chu, Y.-Q., et al. 2012, RAA, 12, 1197
Davis, M., Efstathiou, G., Frenk, C. S., & White, S. D. M. 1985, ApJ, 292,
Drout, M. R., Piro, A. L., Shappee, B. J., et al. 2017, Sci, 358, 1570
Eichler, M., Arcones, A., Kelic, A., et al. 2015, ApJ, 808, 30
Ernst, A., Just, A., Berczik, P., & Olczak, C. 2011, A&A, 536, A64
Ezzeddine, R., Rasmussen, K., Frebel, A., et al. 2020, ApJ, 898, 150
Farouqi, K., Kratz, K. L., Pfeiffer, B., et al. 2010, ApJ, 712, 1359
Foster, T., & Cooper, B. 2010, in ASP Conf. Ser. 438, The Dynamic
   Interstellar Medium: A Celebration of the Canadian Galactic Plane Survey,
   ed. R. Kothes, T. L. Landecker, & A. G. Willis (San Francisco, CA:
   ASP), 16
Frebel, A. 2018, ARNPS, 68, 237
Frebel, A., Casey, A. R., Jacobson, H. R., & Yu, Q. 2013, ApJ, 769, 57
Frebel, A., Christlieb, N., Norris, J. E., et al. 2007, ApJL, 660, L117
Fujimoto, S.-i., Nishimura, N., & Hashimoto, M.-a. 2008, ApJ, 680, 1350
Gaia Collaboration, Brown, A. G. A., Vallenari, A., et al. 2018, A&A, 616, A1
Genova, F., & Schatzman, E. 1979, A&A, 78, 323
Goldstein, A., Veres, P., Burns, E., et al. 2017, ApJL, 848, L14
Grand, R. J. J., Gómez, F. A., Marinacci, F., et al. 2017, MNRAS, 467, 179
Gratton, R. G., Carretta, E., Matteucci, F., & Sneden, C. 2000, A&A, 358, 671
Halevi, G., & Mösta, P. 2018, MNRAS, 477, 2366
Hansen, C. J., Primas, F., Hartman, H., et al. 2012, A&A, 545, A31
Hansen, T. T., Holmbeck, E. M., Beers, T. C., et al. 2018, ApJ, 858, 92
Harfst, S., Gualandris, A., Merritt, D., et al. 2007, NewA, 12, 357
Hawkins, K., & Wyse, R. F. G. 2018, MNRAS, 481, 1028
Haywood, M., Di Matteo, P., Lehnert, M. D., et al. 2018, ApJ, 863, 113
Heger, A., & Woosley, S. E. 2010, ApJ, 724, 341
Helmi, A., Babusiaux, C., Koppelman, H. H., et al. 2018, Natur, 563, 85
Henden, A. A., Templeton, M., Terrell, D., et al. 2016, yCat, 2336, 0
Hesser, J. E. 1978, ApJL, 223, L117
Hill, V., Plez, B., Cayrel, R., et al. 2002, A&A, 387, 560
Holmbeck, E. M., Hansen, T. T., Beers, T. C., et al. 2020, ApJS, 249, 30
Hunter, J. D. 2007, CSE, 9, 90
Iben, Icko, J. 1968, ApJ, 154, 581
Ji, A. P., Frebel, A., Chiti, A., & Simon, J. D. 2016, Natur, 531, 610
Just, A., Yurin, D., Makukov, M., et al. 2012, ApJ, 758, 51
Kang, W., & Lee, S.-G. 2015, TAME: Tool for Automatic Measurement of
   Equivalent-width, Astrophysics Source Code Library, ascl:1503.003
Kennedy, G. F., Meiron, Y., Shukirgaliyev, B., et al. 2016, MNRAS, 460, 240
```

```
Kilpatrick, C. D., Foley, R. J., Kasen, D., et al. 2017, Sci, 358, 1583
Kirby, E. N., Guhathakurta, P., Zhang, A. J., et al. 2016, ApJ, 819, 135
Li, H.-N., Aoki, W., Honda, S., et al. 2015, RAA, 15, 1264
Li, S., Liu, F. K., Berczik, P., Chen, X., & Spurzem, R. 2012, ApJ, 748, 65
Lindegren, L., Hernández, J., Bombrun, A., et al. 2018, A&A, 616, A2
Mardini, M. K., Li, H., Placco, V. M., et al. 2019a, ApJ, 875, 89
Mardini, M. K., Placco, V. M., Taani, A., Li, H., & Zhao, G. 2019b, ApJ,
Marinacci, F., Pakmor, R., & Springel, V. 2014, MNRAS, 437, 1750
Marinacci, F., Vogelsberger, M., Pakmor, R., et al. 2018, MNRAS, 480,
McMillan, P. J. 2011, MNRAS, 414, 2446
McMillan, P. J. 2017, MNRAS, 465, 76
Meiron, Y., Webb, J. J., Hong, J., et al. 2020, arXiv:2006.01960
Mirizzi, A. 2015, PhRvD, 92, 105020
Miyamoto, M., & Nagai, R. 1975, PASJ, 27, 533
Myeong, G. C., Vasiliev, E., Iorio, G., Evans, N. W., & Belokurov, V. 2019,
           , 488, 1235
Nadyozhin, D. K., & Panov, I. V. 2007, AstL, 33, 385
Naidu, R. P., Conroy, C., Bonaca, A., et al. 2020, ApJ, 901, 48
Naiman, J. P., Pillepich, A., Springel, V., et al. 2018, MNRAS, 477, 1206
Navarro, J. F., Frenk, C. S., & White, S. D. M. 1995, MNRAS, 275, 56
Nelson, D., Pillepich, A., Springel, V., et al. 2018, MNRAS, 475, 624
Nelson, D., Pillepich, A., Springel, V., et al. 2019a, MNRAS, 490, 3234
Nelson, D., Springel, V., Pillepich, A., et al. 2019b, ComAC, 6, 2
Neugebauer, G., Habing, H. J., van Duinen, R., et al. 1984, ApJL, 278, L1
Nishimura, N., Sawai, H., Takiwaki, T., Yamada, S., & Thielemann, F. K.
   2017, ApJL, 836, L21
Nishimura, N., Takiwaki, T., & Thielemann, F.-K. 2015, ApJ, 810, 109
Nitadori, K., & Makino, J. 2008, NewA, 13, 498
Noguchi, K., Aoki, W., Kawanomoto, S., et al. 2002, PASJ, 54, 855
Norris, J. 1986, ApJS, 61, 667
Obergaulinger, M., Just, O., & Aloy, M. A. 2018, JPhG, 45, 084001
Pillepich, A., Nelson, D., Hernquist, L., et al. 2018, MNRAS, 475, 648
Pillepich, A., Nelson, D., Springel, V., et al. 2019, MNRAS, 490, 3196
Placco, V. M., Frebel, A., Beers, T. C., & Stancliffe, R. J. 2014, ApJ,
  797, 21
Placco, V. M., Holmbeck, E. M., Frebel, A., et al. 2017, ApJ, 844, 18
Placco, V. M., Santucci, R. M., Yuan, Z., et al. 2020, ApJ, 897, 78
Poole, G. B., Mutch, S. J., Croton, D. J., & Wyithe, S. 2017, MNRAS,
Qian, Y.-Z. 2014, JPhG, 41, 044002
Rodriguez-Gomez, V., Genel, S., Vogelsberger, M., et al. 2015, MNRAS,
  449, 49
Roederer, I. U., Hattori, K., & Valluri, M. 2018, AJ, 156, 179
Roederer, I. U., Preston, G. W., Thompson, I. B., et al. 2014, AJ, 147, 136
Roederer, I. U., Sakari, C. M., Placco, V. M., et al. 2018, ApJ, 865, 129
Rosswog, S., Davies, M. B., Thielemann, F. K., & Piran, T. 2000, A&A,
   360, 171
Sakari, C. M., Placco, V. M., Farrell, E. M., et al. 2018a, ApJ, 868, 110
Sakari, C. M., Placco, V. M., Hansen, T., et al. 2018b, ApJL, 854, L20
Sakari, C. M., Roederer, I. U., Placco, V. M., et al. 2019, ApJ, 874, 148
Sato, K. 1974, PThPh, 51, 726
Savchenko, V., Ferrigno, C., Kuulkers, E., et al. 2017, ApJL, 848, L15
Schönrich, R., Binney, J., & Dehnen, W. 2010, MNRAS, 403, 1829
Searle, L., & Zinn, R. 1978, ApJ, 225, 357
Shappee, B. J., Simon, J. D., Drout, M. R., et al. 2017, Sci, 358, 1574
Siegel, D. M., Barnes, J., & Metzger, B. D. 2019, Natur, 569, 241
Skrutskie, M. F., Cutri, R. M., Stiening, R., et al. 2006, AJ, 131, 1163
Sneden, C., Cowan, J. J., & Gallino, R. 2008, ARA&A, 46, 241
Sneden, C., Cowan, J. J., Lawler, J. E., et al. 2003, ApJ, 591, 936
Sneden, C., McWilliam, A., Preston, G. W., et al. 1996, ApJ, 467, 819
Sneden, C. A. 1973, PhD thesis, The Univ. Texas at Austin
Soares-Santos, M., Holz, D. E., Annis, J., et al. 2017, ApJL, 848, L16
Sobeck, J. S., Kraft, R. P., Sneden, C., et al. 2011, AJ, 141, 175
Sommer-Larsen, J., Beers, T. C., Flynn, C., Wilhelm, R., & Christensen, P. R.
   1997, ApJ, 481, 775
Spite, M., Cayrel, R., Hill, V., et al. 2006, A&A, 455, 291
Springel, V., Pakmor, R., Pillepich, A., et al. 2018, MNRAS, 475, 676
Symbalisty, E., & Schramm, D. N. 1982, ApL, 22, 143
Symbalisty, E. M. D., Schramm, D. N., & Wilson, J. R. 1985, ApJL, 291,
Thielemann, F. K., Arnould, M., & Hillebrandt, W. 1979, A&A, 74, 175
Thielemann, F. K., Eichler, M., Panov, I. V., & Wehmeyer, B. 2017, ARNPS,
   67, 253
```

Thomas, H. C. 1967, ZA, 67, 420

```
Tody, D. 1986, Proc. SPIE, 627, 733
```

Tody, D. 1993, in ASP Conf. Ser. 52, Astronomical Data Analysis Software and Systems II, ed. R. J. Hanisch, R. J. V. Brissenden, & J. Barnes (San Francisco, CA: ASP), 173

van der Walt, S., Colbert, S. C., & Varoquaux, G. 2011, CSE, 13, 22 Vasiliev, E. 2019, MNRAS, 482, 1525

Virtanen, P., Gommers, R., Oliphant, T. E., et al. 2020, Nature Methods, 17, 261

Wang, L., Berczik, P., Spurzem, R., & Kouwenhoven, M. B. N. 2014, ApJ, 780, 164

White, S. D. M., & Rees, M. J. 1978, MNRAS, 183, 341

Witti, J., Janka, H. T., & Takahashi, K. 1994, A&A, 286, 841

Zhao, G., Chen, Y.-Q., Shi, J.-R., et al. 2006, ChJAA, 6, 265 Zhao, G., Zhao, Y.-H., Chu, Y.-Q., Jing, Y.-P., & Deng, L.-C. 2012, RAA, 12, 723

Zhong, S., Berczik, P., & Spurzem, R. 2014, ApJ, 792, 137